Article

Open Access | Vita Microbiology

Pathway deciphering and heterologous production of pyrethrins

Yi Li[1#], Xiaochun Xiao[2#], Shun Wen[2#], Yao Zhi[2], Fangfang Chen[2], Yan Yao[2], Xueting Fang[2], Jing Yang[2], Ranjun Li[2], Denghong Yan[2], Kexin Liu[3], Qijun Jiang[3], Kun Shen[2], Anwei Hou[4], Zixin Deng[1,2], Li Lu[*2], Tiangang Liu[*1]

Natural pyrethrins, extracted from pyrethrum (*Tanacetum cinerariifolium*) flowers, are natural insecticides distinguished by their low toxicity, environmental safety, and reduced risk of pest resistance, advantages unmatched by synthetic pyrethroids. However, the geographical restriction of pyrethrum cultivation and the high cost of plant extraction have limited their supply, leaving synthetic pyrethroids to dominate a substantial share of the global insecticide market. Sustainable microbial production could relieve this supply bottleneck, but key steps in the pyrethrin biosynthetic pathway have remained elusive. Here, we report a high-quality genome of pyrethrum and reconstruct the pyrethrin biosynthetic pathway. We identify a specialized β-oxidation process essential for jasmolone formation, and a glycosylation modification of chrysanthemic acid that precedes ester condensation. We further discover a terpene synthase with dephosphorylation activity that enhances chrysanthemol production and thereby improves pathway efficiency. Reconstitution of the pathway in *Nicotiana benthamiana* yielded four pyrethrin congeners (pyrethrin I/II and jasmolin I/II), while modular reconstruction of the jasmolin I branch in *Saccharomyces cerevisiae* achieved a titer of 1.22 mg/L in shake-flask fermentation. These findings fill the remaining gaps in the pyrethrin biosynthetic pathway and enable microbial production, opening a sustainable route to a safer, more environmentally benign class of insecticides.

https://doi.org/10.2738/vita.microbiology.2026.10.0005

INTRODUCTION

Pyrethrin insecticides are derived from the plant *Tanacetum cinerariifolium* (*T. cinerariifolium*). In the early 1920s, natural pyrethrins were identified as the active ingredients of pyrethrum, enabling the complete structural characterization of all six natural compounds as monoterpenoid esters[1]. As contact neurotoxins, they rapidly disrupt the insect nervous system, causing muscle paralysis, immobilization, and death. Natural pyrethrins exhibit low toxicity to mammals and undergo rapid photodegradation in the environment, with a half-life of only 2 to 48 h[2,3]. Synthetic pyrethroids, including permethrin, tetramethrin, cypermethrin, and cyfluthrin, were developed to overcome the rapid photodegradation of natural pyrethrins[4]. Pyrethroids are now among the most widely used insecticides in agriculture and household products worldwide, holding a substantial share of the modern insecticide market[5]. However, synthetic pyrethroids can persist in soil for weeks or months, leading to environmental accumulation, ecological hazards, and growing resistance in pests. Notably, natural pyrethrins remain effective against certain pests that have developed resistance to synthetic pyrethroids[6-9].

Currently, producing natural pyrethrin insecticides relies on large-scale farming of pyrethrum flowers. This plant exhibits optimal growth and highest pyrethrin yields at high altitudes near the equator[10]. As a result, commercial production is limited to only a few regions such as East Africa, Tasmania in Australia, and Yunnan in China. This limited supply makes natural pyrethrins rare and valuable, creating an urgent need to develop alternative production methods.

Over the past 20 years, genetic and molecular studies of *T. cinerariifolium* have elucidated multiple steps in the pyrethrin biosynthetic pathway[11-21]. Briefly, pyrethrin biosynthesis can be divided into three stages: the synthesis of the acid moiety, the synthesis of the alcohol moiety, and their subsequent condensation (Fig. 1). The biosynthesis of the acid moiety originates from the plastidial terpenoid pathway. Dimethylallyl diphosphate (DMAPP) is converted to chrysanthemyl diphosphate (CDP) by chrysanthemyl diphosphate synthase (TcCDS)[11]. CDP is then dephosphorylated to chrysanthemol, a reaction that has been attributed to a secondary, low-efficiency activity of TcCDS, or is routed through chrysanthemyl monophosphate (CMP) by the Nudix-family phosphatase TcNudix1 and likely requires an additional phosphohydrolase to complete[12]. Chrysanthemol is oxidized to chrysanthemic acid by alcohol dehydrogenase (TcADH2) and aldehyde dehydrogenase (TcALDH1)[13]. As a branch point, chrysanthemol can also be hydroxylated by chrysanthemol 10-hydroxylase (TcCHH)

1. State Key Laboratory of Microbial Metabolism, Joint International Research Laboratory of Metabolic & Developmental Sciences, School of Life Sciences and Biotechnology, Shanghai Jiao Tong University, Shanghai, China. 2. State Key Laboratory of Hybrid Rice, School of Pharmaceutical Sciences, Wuhan University, Wuhan, Hubei, China. 3. Yunnan Nanbao Biotechnology Co., Ltd., Yuxi, Yunnan, China. 4. Tianjin Institute of Industrial Biotechnology, Chinese Academy of Sciences, Tianjin, China. #These authors contributed equally to this work. *Correspondence: Li Lu (luliwhu@whu.edu.cn), Tiangang Liu (liutiangang@sjtu.edu.cn)

Received: August 5, 2026; Accepted: October 28, 2026; Published: November 13, 2026

and subsequently oxidized by TcADH2 and TcALDH1 to form 10-carboxychrysanthemol[14], which is then methylated by the 10-carboxychrysanthemic acid methyltransferase (TcCCMT) to yield pyrethric acid[14] (Fig. 1a).

In contrast, the biosynthesis of the alcohol moiety remains less clearly defined. Its precursor, α-linolenic acid (α-LeA), is thought to be cyclized to form 12-oxo-phytodienoic acid (*cis*-OPDA), which may then undergo β-oxidation, isomerization, and decarboxylation to yield *cis*-jasmone[15]. However, the catalytic mechanisms underlying this transformation remain elusive. *cis*-jasmone is hydroxylated by the jasmone hydroxylase (TcJMH) to form jasmolone[16], which is subsequently desaturated by pyrethrolone synthase (TcPYS) to generate pyrethrolone[17]. The biosynthetic mechanism of cinerolone remains unreported (Fig. 1b). Ultimately, two acid moieties and three alcohol moieties are condensed by the Gly-Asp-Ser-Leu (GDSL) lipase-like protein (TcGLIP) to form the six natural pyrethrins[18,19] (Fig. 1c), although whether coenzyme A (CoA) activation of the acid moiety is required remains unclear.

Although the pyrethrin biosynthetic pathway remains incompletely elucidated, significant advances have been made in recent years, including production of the acid moiety in *Nicotiana benthamiana* (*N. benthamiana*) and tomato[14,20,21], the efficient biosynthesis of chrysanthemic acid in *Escherichia coli* (*E. coli*) through metabolic engineering strategies[22,23], and the discovery of transcription factors TcbZIP60 and TcMYC2 that regulate pyrethrin biosynthesis[24,25]. However, critical gaps remain in our understanding of pyrethrin biosynthesis, including the fundamental mechanisms underlying the low efficiency of acid moiety biosynthesis, the biosynthesis of *cis*-jasmone, and whether CoA activation is essential for the condensation reaction. The absence of key enzymes and unclear mechanisms hinder complete microbial heterologous synthesis, making systematic pathway elucidation essential for efficient production.

In this study, we combined high-quality genome sequencing of *T. cinerariifolium* with comprehensive transcriptome analysis to systematically identify previously uncharacterized enzymes of the pyrethrin biosynthetic pathway. Using multi-host screening and module-by-module pathway reconstruction, we functionally characterized three previously unannotated enzymes. Having established these enzyme functions and reconstituted routes to multiple pyrethrin congeners (pyrethrin I/II and jasmolin I/II) in *N. benthamiana*, we stepwise reconstructed the pathway

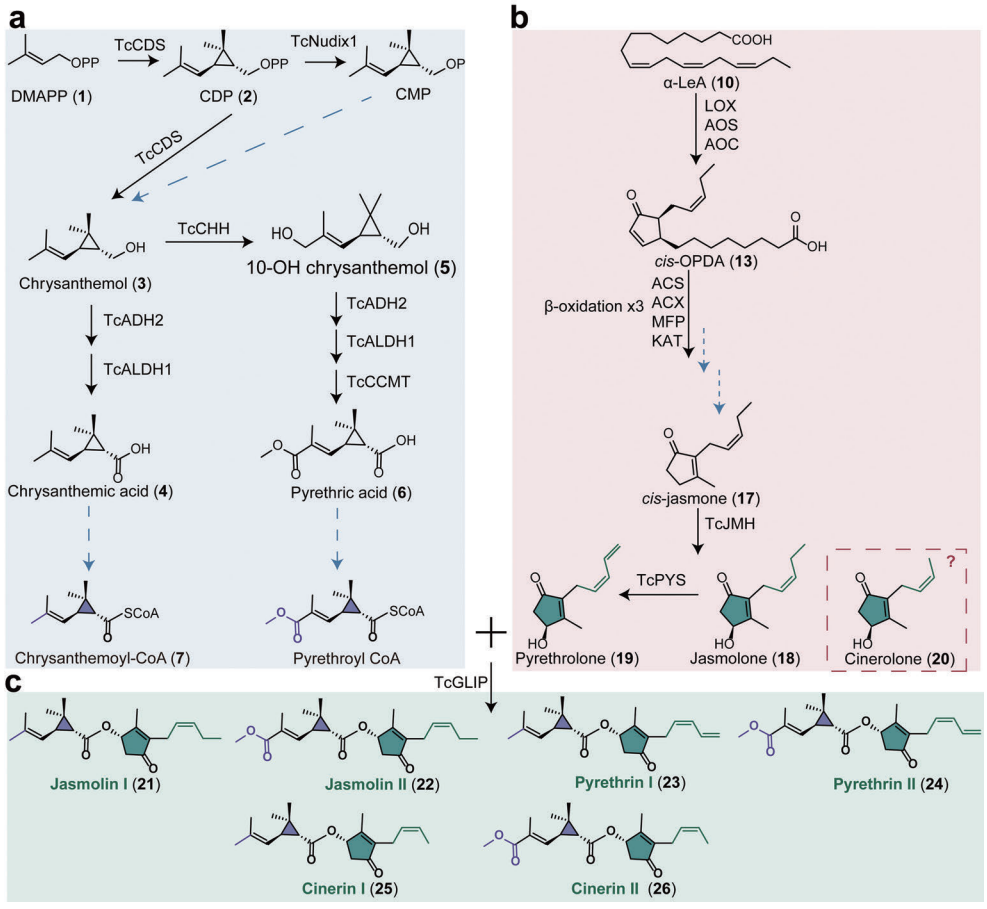


Fig. 1 Proposed pyrethrin biosynthetic pathway. The pathway can be divided into three stages: **a** The biosynthesis of the acid moiety, which originates from the terpene precursor DMAPP. **b** The biosynthesis of the alcohol moiety, derived from α-LeA. **c** Condensation of the acid and alcohol moieties. Based on this classification, pyrethrins containing chrysanthemic acid as the acid moiety are classified as Type I, whereas those containing pyrethric acid are classified as Type II. The blue dashed arrows indicate catalytic steps that have been proposed in previous studies but not yet experimentally confirmed. The red dashed box highlights the biosynthetic step leading to cinerolone, for which the pathway remains uncertain.

modules in *Saccharomyces cerevisiae* (*S. cerevisiae*) to enable fermentative jasmolin I production, providing a starting point for strain optimization and scalable production.

RESULTS

Genome sequencing and pyrethrin accumulation in *T. cinerariifolium*

Natural pyrethrins consist of six esters formed by the conjugation of two monoterpenoids (chrysanthemic acid and pyrethric acid) and three rethrolones (pyrethrolone, jasmolone, and cinerolone) (Fig. 1c). Comparative profiling across various plant tissues and flower developmental stages revealed that chrysanthemic acid and its corresponding esters, jasmolin I and pyrethrin I, were most abundant in disk flowers, followed by jasmolin II (Fig. 2a). To identify genes involved in the pyrethrin biosynthetic pathway, we performed genomic and transcriptomic sequencing. Using 491.87 Gb of Illumina, 393.04 Gb of PacBio Sequel II HiFi long-read, and 693.50 Gb of Illumina Hi-C data (Supplementary Table S1), we assembled a high-quality genome of *T. cinerariifolium*. The final assembly had a total size of 7.71 Gb, consisting of 160 sequences (including 9 chromosome-level scaffolds and 151 supercontigs), and achieved an N50 of 866.94 Mb (Fig. 2b; Supplementary Tables S2, S3). Benchmarking Universal Single Copy Orthologs (BUSCO) analysis based on plant gene models showed that its completeness was 97.3%, indicating relatively high completeness of the assembled *T. cinerariifolium* genome (Supplementary Table S4). By combining transcriptomic data, protein sequences from closely related species, and *de novo* prediction, we predicted a total of 64,171 protein-coding genes. Functional annotation against multiple gene function databases successfully assigned putative functions to 60,832 genes (94.80%) (Supplementary Table S5). A comparative genomic analysis with the genomes of 11 other plant species (Fig. 2c; Supplementary Fig. S1) uncovered 8,527 species-specific gene families in *T. cinerariifolium*, encompassing 17,454 genes (Supplementary Table S6). Further Kyoto Encyclopedia of Genes and Genomes (KEGG) enrichment analysis highlighted metabolism-related adaptations (Supplementary Fig. S2). Phylogenetic reconstruction using 215 highly conserved single-copy orthologs dated the divergence of *T. cinerariifolium* from its closely related Asteraceae sister lineages (e.g., *Artemisia annua*, *Chrysanthemum lavandulifolium*) to approximately 7.9 million years ago (Mya) (Fig. 2c). Furthermore, we identified significant gene family dynamics, with 1,173 families (3,036 genes) undergoing expansion and 1,848 families (2,133 genes) undergoing contraction along the *T. cinerariifolium* lineage (Fig. 2c; Supplementary Table S7). Notably, these evolutionarily dynamic families were predominantly enriched in pathways such as “fatty acid degradation/biosynthesis” and “linoleic acid metabolism”

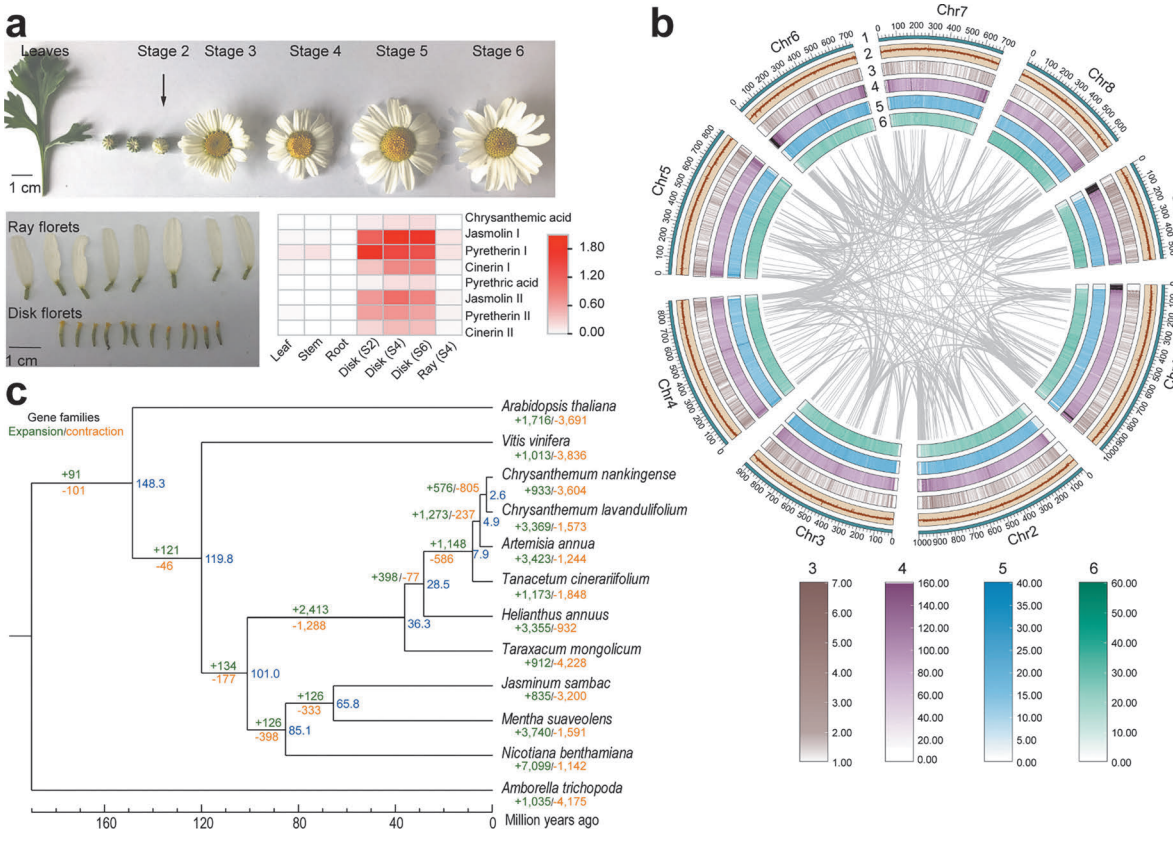


Fig. 2 Pyrethrins tissue distribution, genome sequencing, and evolution of *T. cinerariifolium*. **a** Relative quantification of pyrethrins across various plant tissues and flower developmental stages. **b** Genome sequencing of *T. cinerariifolium*. The linking lines in the circle represent synteny of paralogous sequences in the genome. Outermost to innermost tracks indicate the (1) pseudochromosomes, (2) GC content density, (3) gene density, (4) TE density, (5) Copia LTR density, and (6) Gypsy LTR density. **c** Phylogenetic tree showing the divergence times and gene family evolution across 12 plant species. The values at the nodes indicate divergence times in million years ago (Mya). Green indicates gene family expansion (increase in number); orange indicates gene family contraction (decrease in number).

(Supplementary Figs. S3 and S4), suggesting that *T. cinerariifolium* has evolved distinct regulatory or metabolic features in fatty acid-derived secondary metabolism (such as pyrethrin biosynthesis) compared to its relatives.

A terpene synthase acts as a dephosphatase in chrysanthemic acid biosynthesis

TcCDS catalyzes the first step in the biosynthesis of these monoterpenoids by condensing two molecules of DMAPP (**1**). It has also been proposed to perform additional cleavage of the diphosphate group, thereby generating chrysanthemol (**3**)—the branch point intermediate for the synthesis of both chrysanthemic acid (**4**) and pyrethric acid (**6**) (Fig. 3a). However, when *TcCDS* was expressed in a previously constructed high-DMAPP-producing yeast chassis strain JCR27[26,27], no chrysanthemol (**3**) was detected (Fig. 3b). The gene encoding a Nudix-family phosphatase, *TcNudix1*, which was reported to dephosphorylate CDP (**2**) to CMP[12], was co-expressed

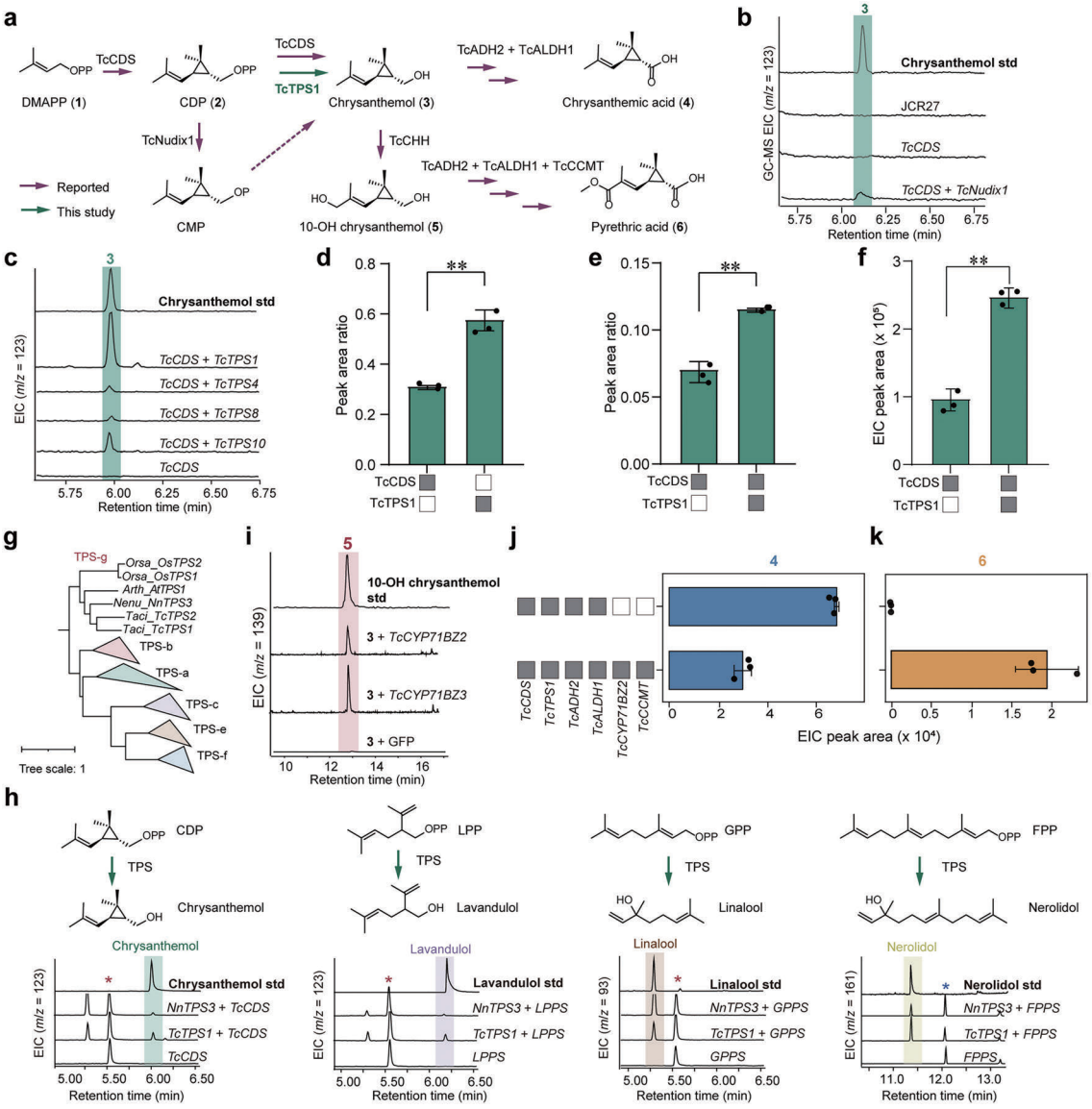


Fig. 3 Identification of a terpene synthase that enhances chrysanthemic acid biosynthesis. a Biosynthetic scheme of chrysanthemic acid (**4**) and pyrethric acid (**6**). **b** Gas chromatography-mass spectrometry (GC-MS) analysis of yeast expressing *TcCDS* and *TcNudix1* on high-copy plasmids. **c** Identification of terpene synthases (TPSs) capable of catalyzing the dephosphorylation of chrysanthemol (**3**). **d** Comparison of the efficiency of TcCDS and TcTPS1 in catalyzing the formation of chrysanthemol (**3**) from CDP (**2**). **e** Comparison of the efficiency of TcCDS in catalyzing formation of chrysanthemol (**3**) from DMAPP (**1**) in the presence and absence of TcTPS1. Quantification was based on the peak area ratio of chrysanthemol (**3**) to internal standard. **f** Co-expression of *TcTPS1* and *TcCDS* increases chrysanthemol (**3**) production in *N. benthamiana*. Statistical significance for **d**–**f** was determined by two-tailed Welch's *t*-test ($n = 3$, $^{**}p < 0.01$). **g** Phylogenetic analysis of *TPS* gene families from *A. thaliana*, *O. sativa*, *N. nucifera*, and *T. cinerariifolium*[30]. **h** GC-MS analysis of products from yeast strain JCR27 co-expressing *TcTPS1* or *NnTPS3* with *TcCDS*, *LPPS*, *GPPS*, and *FPPS*, respectively. Products were identified using commercial standards. Red and blue asterisks denote yeast endogenous metabolites phenethyl alcohol and dodecanoic acid, respectively; peaks at 5.25 min represent linalool formed from yeast endogenous GPP catalyzed by TPS. **i** Functional characterization of *TcCYP71BZ2* and *TcCYP71BZ3* as TcCHHs; GFP served as a negative control. **j**–**k** *De novo* production of chrysanthemic acid (**4**) and pyrethric acid (**6**) in *N. benthamiana* by transient co-expression of indicated genes (mean ± SD, $n = 3$).

with *TcCDS* in the JCR27 strain. This combination yielded only trace amounts of chrysanthemol (**3**) (Fig. 3b). These findings indicate that although TcCDS can catalyze the formation of chrysanthemol (**3**) from DMAPP (**1**), the reaction proceeds with limited efficiency, suggesting that additional enzymes (e.g., phosphatase) might be required to promote this catalytic process[12,13].

In monoterpenoid biosynthesis, certain terpene synthases (TPS) have been reported to exhibit dephosphorylation activity[28]. Firstly, using the Hidden Markov Models (HMMs) search based on the Pfam ID (PF01397 and PF03936)[29,30], we preliminarily identified eighty-three *TPS* genes from the *T. cinerariifolium* genome. Subsequently, we performed transcriptome sequencing of various pyrethrum tissues (leaf, root, stem, flower, etc.). Based on co-expression analysis, we screened for *TPS* genes that showed significant co-expression (correlation coefficient > 0.7) with *TcCDS*, the core gene responsible for chrysanthemol (**3**) biosynthesis. This led to the final identification of eighteen high-confidence *TPS* candidate genes (Supplementary Fig. S5 and Table S8). When co-expressed with *TcCDS* in the yeast chassis strain JCR27, four of these *TPS* genes (*TcTPS1*, *TcTPS4*, *TcTPS8*, and *TcTPS10*) led to the detection of chrysanthemol (**3**), among which *TcTPS1* showed the highest efficiency (Fig. 3c).

To further validate the dephosphorylation activity of TcTPS1, we subsequently expressed and purified TcTPS1 in *E. coli*, confirming its capacity to catalyze the dephosphorylation of CDP (**2**) to chrysanthemol (**3**) *in vitro*, yielding 1.85-fold higher product levels than TcCDS alone (Fig. 3d; Supplementary Fig. S6a). Moreover, when DMAPP (**1**) was used as the substrate, the combination of TcCDS and TcTPS1 increased chrysanthemol (**3**) production by 1.66-fold compared to TcCDS alone (Fig. 3e; Supplementary Fig. S6a). Kinetic analysis revealed that the catalytic efficiency (k_{cat}/K_m) of TcTPS1 in converting CDP (**2**) to chrysanthemol (**3**) was 3.15 $mmol^{-1}s^{-1}$, which was 3.12-fold higher than the reported catalytic efficiency of TcCDS (1.01 $mmol^{-1}s^{-1}$)[31] (Supplementary Fig. S6b). Transient expression in *N. benthamiana* leaves further confirmed that the inclusion of TcTPS1 significantly enhanced the catalytic efficiency of TcCDS, leading to 2.55-fold higher chrysanthemol (**3**) yields (Fig. 3f). TcCDS exhibits low hydrolytic efficiency toward CDP (**2**), despite its ability to efficiently synthesize CDP (**2**) from DMAPP (**1**). This dual activity profile combines efficient CDP (**2**) synthesis with only limited dephosphorylation. As a result, cooperation with TcTPS1 enhanced catalytic efficiency for chrysanthemol (**3**) production. Subcellular localization analysis confirmed co-localization of TcCDS and TcTPS1 in plastids (Supplementary Fig. S6c), which was further validated by luciferase complementation assays *in planta* (Supplementary Fig. S7). The discovery of TcTPS1 as a functional partner that compensates for TcCDS's hydrolytic limitation may have implications for metabolic engineering applications.

A phylogenetic analysis of terpene synthase gene families in pyrethrum, *Arabidopsis*, rice, and lotus revealed that *TcTPS1* belongs to the TPS-g subfamily (Fig. 3g). The TPS-g subfamily constitutes an angiosperm-specific lineage of *TPS* genes, characterized by functional diversification and serving as a key driver of the evolutionary expansion of plant secondary metabolic pathways[30]. Inspired by the dephosphorylation activity of TcTPS1 toward CDP (**2**), we investigated whether TcTPS1 could dephosphorylate other phosphorylated small-molecule substrates. For comparison, we also examined *NnTPS3*, a TPS-g member from lotus[32]. When co-expressed with canonical and non-canonical precursor synthases for monoterpenes and sesquiterpenes, which include *TcCDS*, *LPPS*[33], *GPPS*[34], and *FPPS*[27], both *TcTPS1* and *NnTPS3* produced dephosphorylated and hydroxylated products, leading to the formation of chrysanthemol (**3**), lavandulol, linalool, and nerolidol (Fig. 3h; Supplementary Figs. S8 and S9). These results demonstrate that *TcTPS1* effectively improves the catalytic efficiency of chrysanthemol (**3**) production. Moreover, they support the possibility that the plant TPS-g subfamily may possess broad dephosphorylation activity beyond their established roles in terpenoid formation.

Chrysanthemic acid (**4**) and pyrethric acid (**6**) are two constituent monoterpenoids of pyrethrins, biosynthetically originating from chrysanthemol (**3**) (Fig. 3a). A previously reported P450 (TcCHH) was proposed to hydroxylate the C-10 position of chrysanthemol (**3**) to yield 10-OH chrysanthemol (**5**)[14]. Co-expression analysis identified two additional cytochrome P450 enzymes, TcCYP71BZ2 and TcCYP71BZ3, differing from the previously reported TcCHH by 10 and 3 amino acids, respectively (Supplementary Fig. S10 and Table S9). Genomic analysis revealed that *TcCYP71BZ2* is located adjacent to, but distinct from, the *TcCHH* locus, while *TcCYP71BZ3* resides at a separate genomic location, indicating that these represent paralogous genes rather than allelic variants (Supplementary Fig. S11). Functional analysis in *N. benthamiana* confirmed that both enzymes catalyze chrysanthemol (**3**) to 10-OH chrysanthemol (**5**), as verified by comparison with an in-house synthesized chemical standard (Fig. 3i). By co-expressing *TcCDS*, *TcTPS1*, *TcADH2*, and *TcALDH1* in *N. benthamiana* leaves, we achieved *de novo* production of chrysanthemic acid (**4**) (Fig. 3j; Supplementary Fig. S12a). Furthermore, upon introducing *TcCYP71BZ2* and the previously reported methyltransferase *TcCCMT*[14], we successfully produced pyrethric acid (**6**) (Fig. 3k; Supplementary Fig. S12b).

cis-jasmone biosynthesis through specialized β-oxidation in pyrethrum

cis-jasmone (**17**) serves as a critical volatile defense signal in many plants, being rapidly released upon mechanical wounding or herbivory to repel pests and attract natural enemies[16,35-37]. Although its biosynthesis remains incompletely characterized, it is potentially linked to the jasmonic acid (JA) pathway due to structural similarity. Based on this, previous studies hypothesized that *cis*-jasmone (**17**) might be directly derived from *iso*-OPDA (**14**) via a proposed β-oxidation step to form 3,7-ddh-JA (**16**), followed by decarboxylation (Fig. 4a). In this hypothetical pathway, *iso*-OPDA (**14**) and 3,7-ddh-JA (**16**) are posited as key intermediates[15,38]. However, this mechanistic model lacks experimental validation *in planta*.

In plants, *cis*-OPDA (**13**) is synthesized from α-LeA (**10**) by the sequential action of 13-lipoxygenase (LOX), allene oxide synthase (AOS), and allene oxide cyclase (AOC)[39]. To define this upstream branch in pyrethrum, we performed co-expression analysis with *TcJMH* and *TcPYS*, and obtained ten candidate genes (seven *TcLOX*, two *TcAOS*, and one

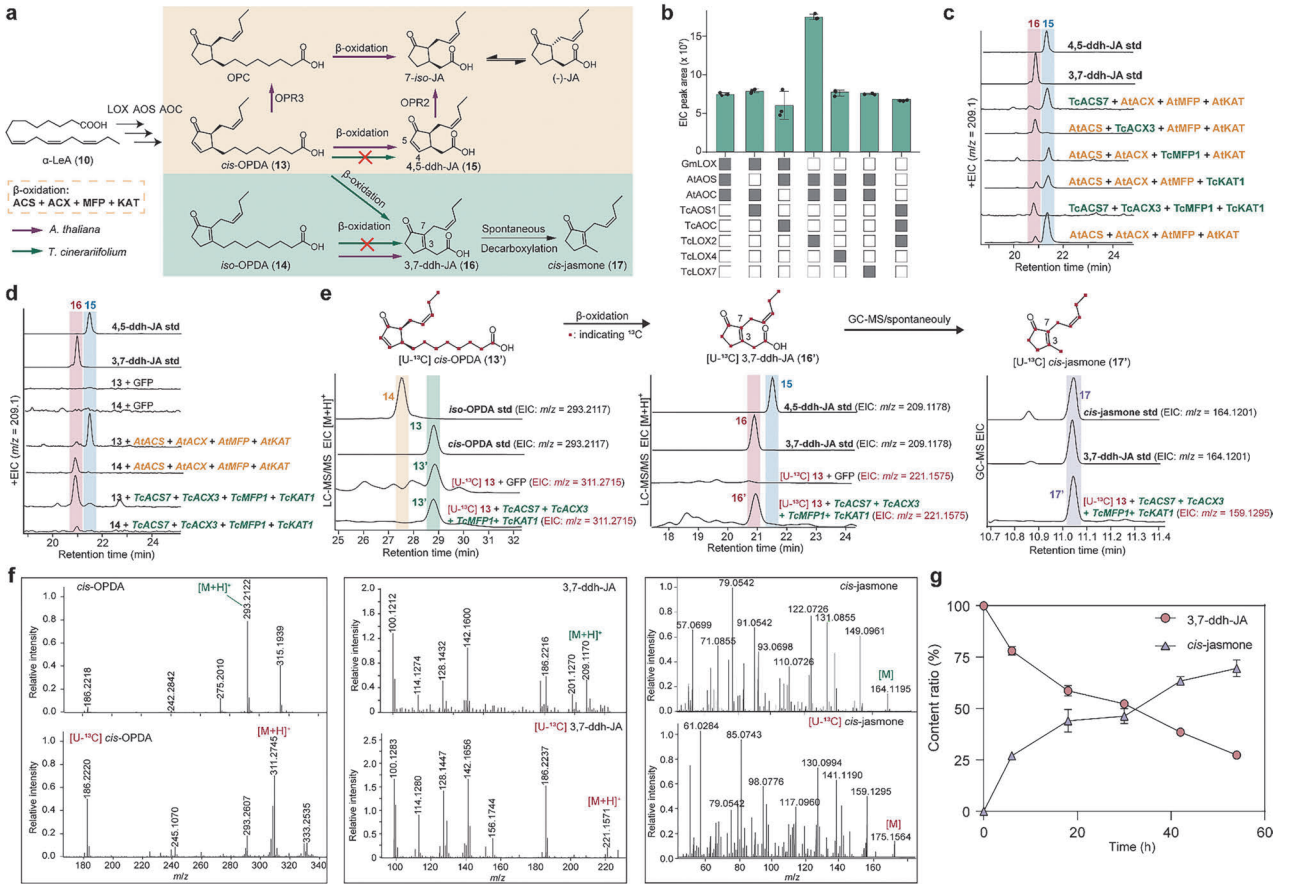


Fig. 4 Specialized β-oxidation resulted in the formation of 3,7-ddh-JA and *cis*-jasmone. a Proposed biosynthetic scheme of *cis*-jasmone (**17**). Light brown: jasmonic acid (JA) pathway reported in *Arabidopsis*; greyish-green: the *cis*-jasmone (**17**) pathway inferred here from substrate-feeding. **b** Recombinant LOX/AOS/AOC convert α-LeA (**10**) to *cis*-OPDA (**13**). (LC-MS EIC, $[M+H]^+ m/z$ = 293.2, *n* = 3). **c** Stepwise replacement of *Arabidopsis* β-oxidases (yellow) with pyrethrum counterparts (green) using *cis*-OPDA (**13**) as substrate. **d** β-oxidases from *A. thaliana* and *T. cinerariifolium* expressed in *N. benthamiana* and incubated with *cis*-OPDA (**13**) and *iso*-OPDA (**14**). GFP served as control. EICs for 4,5-ddh-JA (**15**) and 3,7-ddh-JA (**16**) ($[M+H]^+ m/z$ = 209.1). **e** Pyrethrum β-oxidases convert [U-^{13}C] *cis*-OPDA (**13'**) into [U-^{13}C] 3,7-ddh-JA (**16'**) and [U-^{13}C] *cis*-jasmone (**17'**); unlabelled **13**, **14**, **16**, and **17** were undetectable. EICs: **13** and **14** ($[M+H]^+$ ion; *m/z* = 293.2117), [U-^{13}C] *cis*-OPDA (**13'**) ($[M+H]^+$ ion; *m/z* = 311.2715), [U-^{13}C] 3,7-ddh-JA (**16'**) ($[M+H]^+$ ion; *m/z* = 221.1575), **16** ($[M+H]^+$ ion; *m/z* = 209.1178), **17** ([M] ion; *m/z* = 164.1201), [U-^{13}C] *cis*-jasmone (**17'**) ([M] ion; *m/z* = 175.1564, 159.1295). **f** The MS/MS spectra of **13**, **16**, **17** and their [U-^{13}C] analogues. **g** Time course of **16** spontaneous decarboxylation *in vitro*. The samples were analyzed directly by untargeted LC-MS at 6, 18, 30, 42, and 54 h in DMSO solvent at room temperature (25 °C). Peak-area ratios of **16** and **17** relative to initial **16**.

single-copy *TcAOC*). Subsequent *in vitro* reconstitution assays revealed that only *TcLOX2*, *TcLOX4*, *TcLOX7*, *TcAOS1*, and *TcAOC* catalyzed the formation of *cis*-OPDA (**13**) (Supplementary Fig. S13). Their activities were consistent with those of the previously characterized *GmLOX*, *AtAOS*, and *AtAOC* from soybean and *Arabidopsis*[40] (Fig. 4b; Supplementary Fig. S14). By contrast, the formation of *iso*-OPDA (**14**) has only been reported via *cis*-OPDA (**13**) isomerization by a glutathione transferase 16 (GST16) cloned from the gut of cotton bollworm larvae[41,42], with no known plant pathway. We therefore prepared *cis*-OPDA (**13**) and *iso*-OPDA (**14**) by chemo-enzymatic synthesis for use as both enzymatic substrates and analytical standards (Supplementary Fig. S15a), and used them to screen the candidate genes in pyrethrum genome. However, no pyrethrum gene capable of directly producing *iso*-OPDA (**14**) was identified, and none of pyrethrum *GST* genes displayed *cis*- to *iso*-OPDA isomerase activity (Supplementary Fig. S16).

β-oxidation represents a critical step in jasmonate biosynthesis, dependent on four core enzymes, namely acyl-CoA synthetase (ACS), acyl-CoA oxidase (ACX), multifunctional protein (MFP), and L-3-ketoacyl-CoA thiolase (KAT), which together catalyze three iterative cycles of oxidation to convert *cis*-OPDA (**13**) and OPC (derived from *cis*-OPDA via OPDA reductase, OPR) into 4,5-ddh-JA (**15**) and 7-*iso*-JA, respectively, ultimately yielding JA[43,44] (Fig. 4a). Notably, *iso*-OPDA (**14**) has been shown to undergo β-oxidation in various plants to form 3,7-ddh-JA (**16**), a direct precursor of *cis*-jasmone (**17**)[38]. Based on co-expression network analysis with the identified pathway genes (*TcAOC*, *TcCDS*, and *TcJMH*), we identified twenty-five β-oxidation-related genes from the pyrethrum genome, comprising eight *ACS*, twelve *ACX*, two *MFP*, and three *KAT* genes. To enable unambiguous assignment of their reaction products during functional validation, we synthesized 4,5-ddh-JA (**15**) as a reference standard (Supplementary Fig. S17a–d).

To validate the pyrethrum β-oxidation genes, we adopted a combinatorial replacement strategy in which the four core *Arabidopsis* enzymes (AtACS, AtACX, AtMFP, and AtKAT) served as a reference backbone, and each component was

swapped individually with its pyrethrum counterpart. When assaying the *ACS/MFP/KAT* candidate genes with *cis*-OPDA (**13**), the major product was 4,5-ddh-JA (**15**) (retention time [RT] = 21.5 min), which was consistent with the results from the full *Arabidopsis* control group. Among them, *TcACS7*, *TcMFP1*, and *TcKAT1* exhibited the highest efficiency (Supplementary Fig. S18a, c, d). By contrast, ACX candidate assays (including six enzymes such as TcACX2, TcACX3, and TcACX5) produced a new peak at RT = 20.9 min with identical molecular mass to 4,5-ddh-JA (**15**) (Supplementary Fig. S18b), suggesting an isomeric product. To verify its identity, we enzymatically and chemically synthesized 3,7-ddh-JA (**16**) (Supplementary Fig. S17a–d), confirming that the 20.9-min peak corresponded to 3,7-ddh-JA (**16**). Among six pyrethrum *ACX* genes tested in *N. benthamiana*, *TcACX3* exhibited the highest activity, converting *cis*-OPDA (**13**) specifically into 3,7-ddh-JA (**16**) (Supplementary Fig. S19). Stepwise replacement of *Arabidopsis* β-oxidation enzymes with their pyrethrum counterparts revealed that substituting only AtACX with TcACX3 was sufficient to produce 3,7-ddh-JA (**16**) as the sole product (Fig. 4c; Supplementary Fig. S20a), along with detectable *cis*-jasmone (**17**) (Supplementary Fig. S21).

When four pyrethrum β-oxidation genes (*TcACS7*, *TcACX3*, *TcMFP1*, and *TcKAT1*) were transiently expressed in *N. benthamiana* and incubated with *cis*-OPDA (**13**), they produced almost exclusively 3,7-ddh-JA (**16**), with negligible 4,5-ddh-JA (**15**). Only trace amounts of 3,7-ddh-JA (**16**) were derived from *iso*-OPDA (**14**) (Fig. 4d; Supplementary Fig. S20b). This indicates that β-oxidation genes in pyrethrum simultaneously oxidize *cis*-OPDA (**13**) and isomerize its double-bond position—a previously unrecognized mechanism. Feeding synthesized ^{13}C-labeled *cis*-OPDA (**13'**) (Supplementary Fig. S15a, d) to *N. benthamiana* leaves co-expressing the four genes yielded ^{13}C-labeled 3,7-ddh-JA (**16'**) and its decarboxylation product, ^{13}C-labeled *cis*-jasmone (**17'**), but no labeled *iso*-OPDA (**14'**) or 4,5-ddh-JA (**15'**) (Fig. 4e, f). These data confirm that pyrethrum harbors a specialized β-oxidation system capable of converting *cis*-OPDA (**13**) directly into 3,7-ddh-JA (**16**).

Since *cis*-jasmone (**17**) can arise from spontaneous decarboxylation of 3,7-ddh-JA (**16**)[15,45], we consistently detected *cis*-jasmone (**17**) alongside 3,7-ddh-JA (**16**) *in vitro* with recombinant β-oxidation enzymes, as well as in *N. benthamiana*, and yeast systems (Supplementary Fig. S22). Further incubation of purified 3,7-ddh-JA (**16**) at room temperature confirmed time-dependent decarboxylation to *cis*-jasmone (**17**), reaching approximately 75% conversion after 54 h (Fig. 4g). We further noted that 3,7-ddh-JA (**16**) partially decarboxylates in the GC inlet during GC-MS analysis (Supplementary Fig. S17d); accordingly, 3,7-ddh-JA (**16**) was quantified by LC-MS and the *cis*-jasmone (**17**) signal was used for qualitative assignment only. Collectively, these results indicate that *cis*-jasmone (**17**) is produced via a specialized pathway in pyrethrum (Fig. 4a): α-LeA (**10**) is converted into *cis*-OPDA (**13**) in three enzymatic steps; the specialized β-oxidation cascade, with TcACX as the key determinant, directly transforms *cis*-OPDA (**13**) into 3,7-ddh-JA (**16**) through a coupled oxidation-isomerization reaction; and 3,7-ddh-JA (**16**) finally undergoes spontaneous decarboxylation to yield *cis*-jasmone (**17**).

Glycosylation of chrysanthemic acid is the key step for ester condensation

Ester condensation is the final step in the biosynthesis of the six pyrethrins, yet the activation mechanism enabling this condensation remained to be fully elucidated. A GDSL lipase-like protein (GLIP) isolated from pyrethrum flowers can catalyze, *in vitro*, the condensation of either chrysanthemoyl-CoA or pyrethroyl-CoA with three rethrolones to produce all six natural pyrethrins (Fig. 5a)[18,19]. Using chemically synthesized chrysanthemoyl-CoA (**7**), we confirmed that only chrysanthemoyl-CoA (**7**), but not free chrysanthemic acid (**4**), undergoes condensation with jasmolone (**18**) in the presence of TcGLIP (Fig. 5b; Supplementary Fig. S23a). However, the CoA ligase responsible for activating chrysanthemic acid (**4**) to chrysanthemoyl-CoA (**7**) *in vivo* remains unknown, and the chrysanthemoyl-CoA (**7**) used in prior TcGLIP studies was chemically synthesized[18,19]. To identify this enzyme, we screened candidate CoA ligase genes from pyrethrum that showed co-expression with chrysanthemic acid (**4**) biosynthetic genes and tested their activity *in vitro*. Unfortunately, none of the eight candidates successfully produced chrysanthemoyl-CoA (**7**) (Supplementary Fig. S23b).

During activity screening in *N. benthamiana* leaves, we unexpectedly found that chrysanthemic acid (**4**), when injected into *N. benthamiana* leaves, was converted into metabolites that could serve as substrates for TcGLIP. When these metabolites were incubated with jasmolone (**18**), they underwent enzymatic condensation to yield jasmolin I (**21**) (Fig. 5b). This finding is consistent with prior reports demonstrating that transient co-expression of *TcJMH* and *TcGLIP* genes in *N. benthamiana*, followed by feeding with chrysanthemic acid (**4**) and *cis*-jasmone (**17**) alone (without the addition of an exogenous CoA ligase), is sufficient for the biosynthesis of jasmolin I (**21**)[16,17]. Together, these results indicate that *in planta* modification of chrysanthemic acid (**4**) in *N. benthamiana* is essential for the esterification reaction. LC-MS/MS analysis revealed that chrysanthemic acid (**4**) is further modified into chrysanthemoyl-glucoside (**8**) and chrysanthemoyl-malonylglucoside (**9**) in *N. benthamiana* leaves (Fig. 5c, d; Supplementary Fig. S24a, b), consistent with previous reports[13]. We also identified these glucosylated conjugates of chrysanthemic acid (**4**) in pyrethrum disk flowers (Fig. 5c, d); their abundance changed dynamically during inflorescence development (Supplementary Fig. S24c, d) and correlated significantly with most pyrethrin congeners and with the expression of *TcJMH*, *TcPYS*, *TcUGT1/6*, and *TcGLIP* across tissues (Supplementary Fig. S25). By contrast, chrysanthemoyl-CoA (**7**) was barely detectable in leaves, stems, roots, and inflorescence tissues at different growth stages (Supplementary Fig. S24e, f). These results suggest that chrysanthemoyl-glucoside (**8**) is likely a physiologically relevant acyl donor in pyrethrin biosynthesis, although a role for chrysanthemoyl-CoA (**7**) cannot be fully excluded.

We then selected ten glycosyltransferases that are highly expressed in flowers for functional screening through correlation analysis (Supplementary Fig. S26 and Tables S10, S11). After heterologous expression in *E. coli*, we found that TcUGT1 and TcUGT6 were able to glycosylate chrysanthemic acid (**4**), producing chrysanthemoyl-glucoside (**8**)—a product identical to the modified form of chrysanthemic acid (**4**) previously

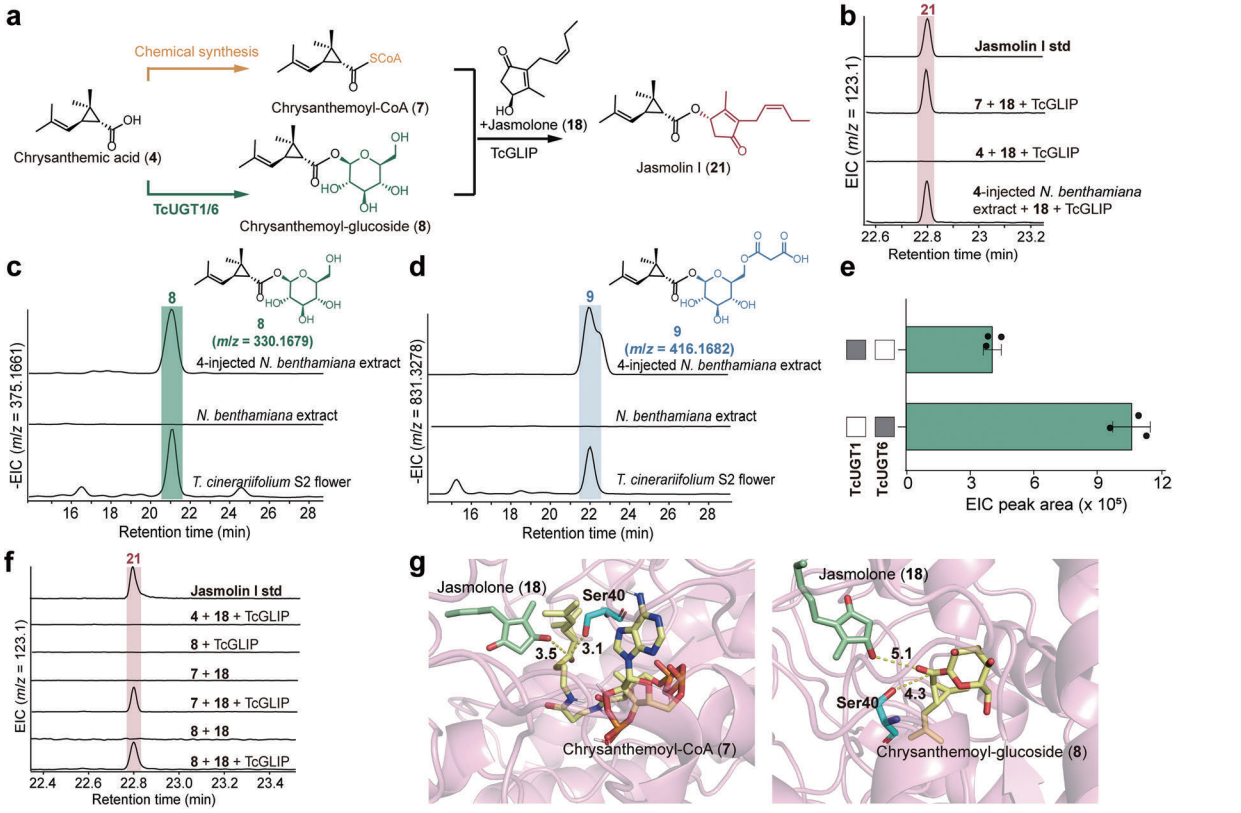


Fig. 5 Glycosylation of chrysanthemic acid is the key step for ester condensation. a Biosynthesis scheme of jasmolin I (**21**) formation via ester condensation. Yellow indicates biosynthetic pathway reported previously; green indicates pathway discovered in this study. **b** GC-MS analysis of jasmolin I (**21**) from TcGLIP reactions with jasmolone (**18**) and chrysanthemoyl-CoA (**7**), chrysanthemic acid (**4**), or **4**-injected *N. benthamiana* extract. **c**, **d** Detection of glucosylated conjugates of **4** in pyrethrum disk flowers and **4**-injected *N. benthamiana* leaves. EIC integrated peak areas for chrysanthemoyl-glucoside (**8**) ($[M+HCOOH-H]^-$ ion; *m/z* = 375.1661), chrysanthemoyl-malonylglucoside (**9**) ($[2M-H]^-$ ion; *m/z* = 831.3278). **e** LC-MS analysis of *in vitro* products from TcUGT1 and TcUGT6 with **4** and UDP-glucose disodium salt. Bar chart, mean ± SD, *n* = 3 biological replicates. **f** GC-MS EIC of TcGLIP-catalyzed reactions with different acyl donors. Experimental group: **8** + **18** + TcGLIP; Control: **4** + **18** + TcGLIP, **8** + TcGLIP, **7** + **18** + TcGLIP, **7** + **18**, and **8** + **18**. Three biological replicates per group. EICs monitored the ion at *m/z* = 123.1, corresponding to jasmolin I (**21**). **g** Schematic models of the TcGLIP catalytic pocket with substrates **7** + **18** (left), or **8** + **18** (right).

detected in *N. benthamiana* leaves (Fig. 5e; Supplementary Fig. S27). We then used purified chrysanthemoyl-glucoside (**8**) as the acyl donor in a TcGLIP-catalyzed condensation with jasmolone (**18**) (Supplementary Fig. S28). TcGLIP produced jasmolin I (**21**) when chrysanthemoyl-CoA (**7**) or chrysanthemoyl-glucoside (**8**) was supplied as donor (Fig. 5f), and accumulation of jasmolin I (**21**) tracked with consumption of chrysanthemoyl-glucoside (**8**) (Supplementary Fig. S29). No product was detected in controls lacking TcGLIP, lacking jasmolone (**18**), or containing free chrysanthemic acid (**4**) instead of an activated acyl donor. This confirms that trace residual chrysanthemic acid (**4**) co-purified with chrysanthemoyl-glucoside (**8**) did not contribute to ester formation (Fig. 5f).

The capacity of TcGLIP to catalyze ester condensation using both the bulky chrysanthemoyl-CoA (**7**) and the smaller chrysanthemoyl-glucoside (**8**) attracted our interest. Typically, the ester condensation of such structurally distinct substrates has been reported to require distinct enzyme families. For instance, in the biosynthesis of plant tropane alkaloids, the esterification of tigloyl-CoA and phenyllactyl glucoside is catalyzed by a BAHD acyltransferase (BAHD-AT, TS)[46] and a serine carboxypeptidase-like acyltransferase (SCPL-AT, LS)[47], respectively. However, we conducted functional characterization on the nine *TcSCPL* genes selected through the co-expression analysis, and found that none of them had any functional significance (Supplementary Fig. S30 and Table S12). To investigate the underlying molecular basis, we predicted the protein structure of TcGLIP and performed molecular docking simulations with each substrate paired with jasmolone (**18**). The results revealed that Ser40 within the conserved N-terminal GDSX motif acts as a nucleophile attacking the ester carbonyl of the substrate (Fig. 5g). The distances between Ser40 and the carbonyl carbon of chrysanthemoyl-CoA (**7**) and chrysanthemoyl-glucoside (**8**) were 3.1 Å and 4.3 Å, respectively. Meanwhile, jasmolone (**18**) was positioned for a second nucleophilic attack, with its hydroxyl oxygen located 3.5 Å and 5.1 Å from the carbonyl carbons of the two substrates, respectively. Both distances fall within the effective nucleophilic attack radius (≤ 5.5 Å). In addition, the TS active site (804.16 $Å^3$) is significantly larger than that of LS (654.58 $Å^3$), consistent with their respective specificities for the bulky tigloyl-CoA and the smaller phenyllactyl glucoside. The volume of GLIP's active pocket (744.91 $Å^3$) is intermediate between them (Supplementary Fig. S31). These results suggest that the broad substrate acceptance of GLIP is enabled by its characteristically open and plastic active pocket.

Reconstitution and combinatorial biosynthesis of multiple pyrethrins in *N. benthamiana*

To validate the functionality of the assembled pathway, we attempted heterologous biosynthesis of multiple pyrethrin congeners (pyrethrin I/II, jasmolin I/II) in *N. benthamiana* through different gene combinations (Fig. 6a). The biosynthetic steps were divided into modules: Group 1, comprising four genes responsible for chrysanthemic acid (**4**) synthesis (*TcCDS*, *TcTPS1*, *TcADH2*, and *TcALDH1*), was combined with the jasmolone hydroxylase gene *TcJMH* and the final esterification enzyme gene *TcGLIP*. Transient co-expression of these genes in *N. benthamiana*, followed by feeding with *cis*-jasmone (**17**), successfully yielded jasmolin I (**21**) (Fig. 6b). Feeding with 3,7-ddh-JA (**16**) also produced jasmolin I (**21**) (Fig. 6b), confirming that 3,7-ddh-JA (**16**) undergoes spontaneous decarboxylation to form *cis*-jasmone (**17**) *in planta*.

Next, we combined Group 2 (the β-oxidation module: *TcACS7*, *TcACX3*, *TcMFP1*, and *TcKAT1*) with Group 1, *TcJMH*, and *TcGLIP*. Transient expression of this set in *N. benthamiana* supplemented with *cis*-OPDA (**13**) successfully generated jasmolin I (**21**) (Fig. 6b). Further extending the pathway, we introduced a total of thirteen genes, including Group 3 (the *cis*-OPDA (**13**) synthesis module: *TcLOX2*, *TcAOS1*, and *TcAOC*) together with Groups 1 and 2, *TcJMH*, and *TcGLIP* into *N. benthamiana* leaves. Supplementation with α-LeA (**10**) enabled the heterologous production of jasmolin I (**21**) (Fig. 6b), demonstrating the functionality of the reconstructed route to jasmolin I (**21**).

Natural pyrethrins comprise six esters formed by conjugating structurally modified chrysanthemic acids with rethrolones (Fig. 1). To diversify the products, we introduced Group 4 genes (*TcCYP71BZ2* and *TcCCMT* for acid modification, and *TcPYS* for rethrolone modification) alongside Group 1, *TcJMH*

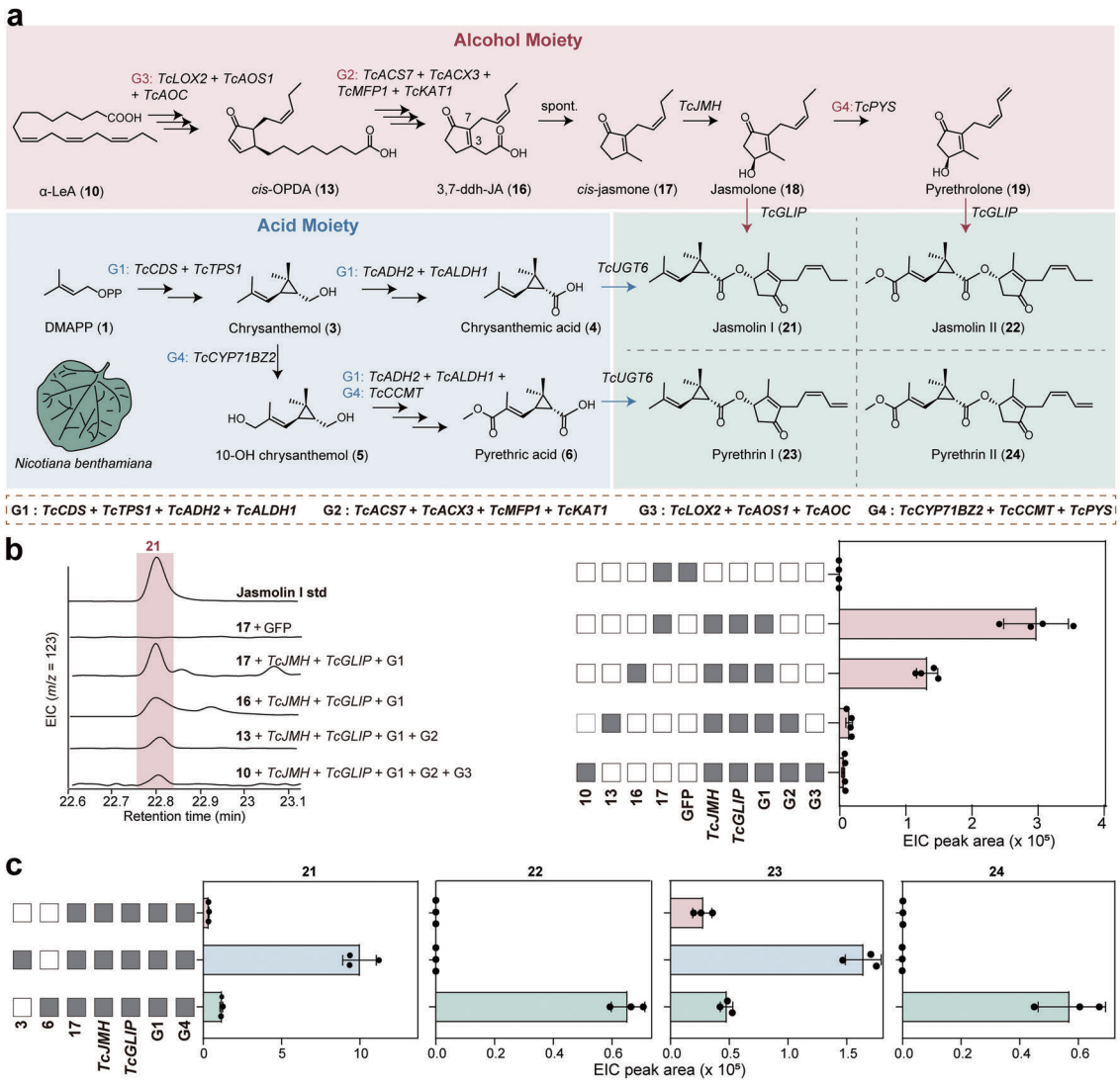


Fig. 6 Reconstruction of biosynthesis of pyrethrins in *N. benthamiana*. **a** Biosynthetic schematic shows the combination of three biosynthetic modules for the engineered production of pyrethrins in *N. benthamiana*. **b** GC-MS chromatograms showing the formation of jasmolin I (**21**) through different combinations of gene groups and substrates. The bar chart (right panel) shows a comparison of the EIC peak areas for compounds produced by the combined pathway genes. Values represent the mean of four biological replicates, with error bars indicating the standard error. **c** GC-MS EIC peak areas of jasmolin I (**21**), jasmolin II (**22**), pyrethrin I (**23**) and pyrethrin II (**24**) produced by different combinations of gene groups and substrates. Data are presented as the mean ± SD of three biological replicates.

and *TcGLIP*. Feeding *cis*-jasmone (**17**) to this engineered background yielded jasmolin I (**21**) (Fig. 6c; Supplementary Fig. S32a). To enhance the supply of chrysanthemic acid (**4**) and its derivatives, we further supplemented the system with the intermediate chrysanthemol (**3**), which enabled the simultaneous production of jasmolin I (**21**) and pyrethrin I (**23**) (Fig. 6c; Supplementary Fig. S32c). Due to the low efficiency of pyrethric acid (**6**) formation, direct feeding of pyrethric acid (**6**) allowed the detection of jasmolin II (**22**) and pyrethrin II (**24**) in *N. benthamiana* leaves (Fig. 6c; Supplementary Fig. S32b, d). Collectively, by incorporating modification enzymes and supplementing key intermediates, we achieved the heterologous biosynthesis of four pyrethrins in *N. benthamiana* (Fig. 6a).

Modular engineering enables heterologous biosynthesis of jasmolin I in yeast

Having reconstituted the pyrethrin biosynthetic pathway and achieved heterologous production of jasmolin I (**21**) from α-LeA (**10**) in *N. benthamiana*, we next sought to establish the same route in a yeast chassis. The overall metabolic engineering strategy was divided into three modules: Module I for chrysanthemic acid (**4**) biosynthesis, Module II for jasmolone (**18**) biosynthesis, and Module III for the formation of chrysanthemoyl-glucoside (**8**) and the final ester condensation (Fig. 7a).

In Module I, we started with the mevalonate (MVA)-overexpressing *S. cerevisiae* strain JCR27[26,27]. Genomic integration of three copies of *TcCDS*, one copy of *TcTPS1*, and three copies of *TcALDH1* and *TcADH2* produced strain J1 (Supplementary Table S13), which produced detectable but very low levels of chrysanthemic acid (**4**) (Fig. 7b; Supplementary Fig. S33). To enhance DMAPP precursor supply, we replaced the native promoter of *ERG20* (yeast FPPS) with the glucose-inducible promoter P_{HXT1} to dynamically downregulate its expression, thereby reducing competitive flux toward endogenous terpenes[48]. The resulting strain J2 showed a substantial increase in chrysanthemic acid (**4**) production, reaching 28.54 mg/L in shake-flask culture (Fig. 7b).

For Module II, we began with a yeast strain 30000B and integrated the high-efficiency *cis*-OPDA (**13**) synthesis genes *GmLOX*, *AtAOS*, and *AtAOC* as a cassette into the *LEU2* locus, generating strain S1 (Supplementary Table S13). Feeding α-LeA (**10**) to S1 successfully resulted in the production

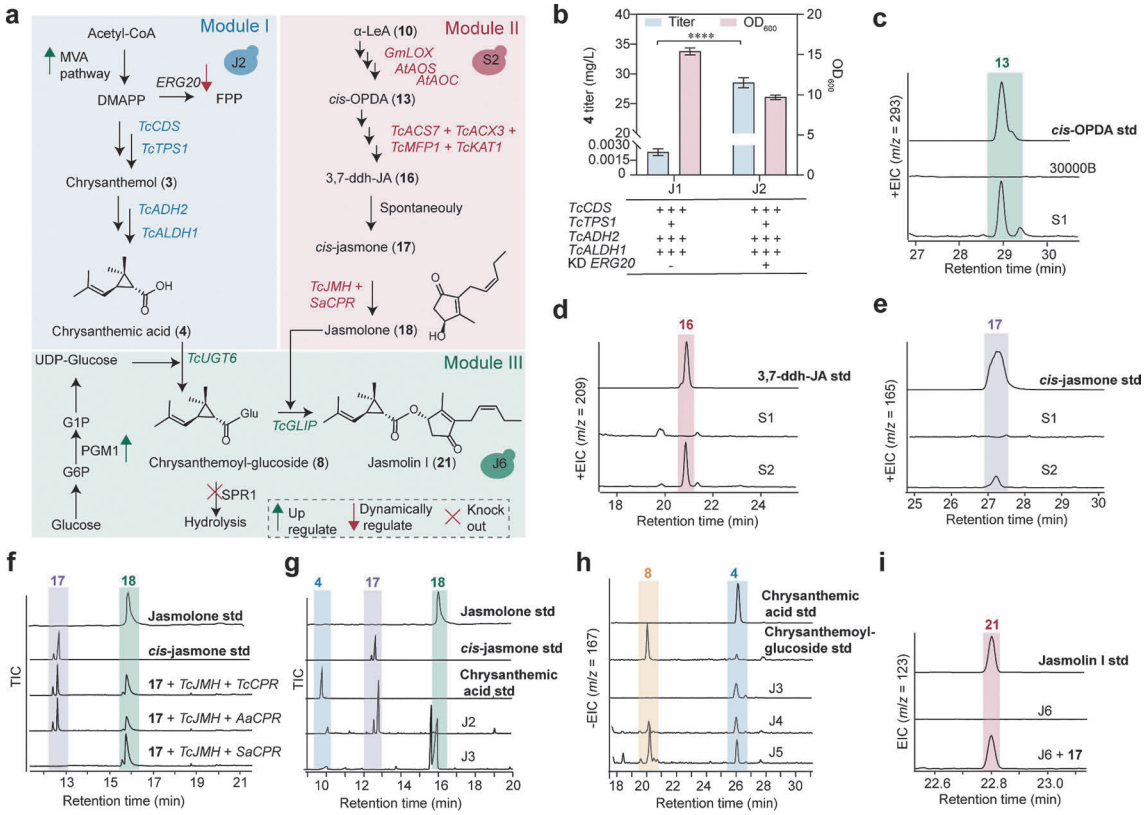


Fig. 7 Modular reconstruction of jasmolin I (21) biosynthetic pathway in *S. cerevisiae*. **a** Schematic of the three-module pathway engineering strategy. Green upward arrows: overexpression of endogenous yeast pathways or genes; red downward arrows: dynamic regulation of endogenous yeast genes; red crosses: knockouts. **b–i** Metabolic profiling of sequentially engineered yeast strains. **b** Chrysanthemic acid (**4**) titers in yeast strains J1 and J2. (72 h culture; LC-MS of supernatant, mean ± SD, $n = 3$, $^{****}p < 0.0001$, Student's *t*-test; OD_{600} measured). Each "+" denotes one integrated gene copy. **c** *cis*-OPDA (**13**) production in yeast strain S1 (expressing *GmLOX/AtAOS/AtAOC*). **d** 3,7-ddh-JA (**16**) in yeast strains S1 and S2 (S2 engineered with *TcACS7*, *TcACX3*, *TcMFP1*, and *TcKAT1*). **e** Detection of *cis*-jasmone (**17**) in yeast strains S1 and S2. **f** Screening plant redox partners to enhance *TcJMH* by whole-cell catalysis. **g** Conversion of *cis*-jasmone (**17**) to jasmolone (**18**) in yeast strains J2 and J3 (J3 engineered with T*cJMH* and *SaCPR*). **h–i** Stepwise engineering from J3 to J6 for jasmolin I (**21**) production. J4 (based on J3) integrates *TcUGT6* and *TcGLIP*; J5 (based on J4) overexpresses *TcUGT6* and *PGM1* while disrupting *SPR1*; J6 (based on J5) knocks out *GAL80* and integrates another copy of *TcGLIP*. Strains were cultured for 96 h with 1.22 mmol/L *cis*-jasmone (**17**) before GC-MS analysis of supernatant.

of *cis*-OPDA (**13**) (Fig. 7c). Subsequently, the β-oxidation genes *TcACS7*, *TcACX3*, *TcMFP1*, and *TcKAT1* were integrated as a second and third cassette into the *YPRCΔ15* and *URA3* loci, producing strain S2 (Supplementary Table S13). Supplementation of S2 with α-LeA (**10**) enabled the production of 3,7-ddh-JA (**16**) (Fig. 7d). Extending the fermentation to four days further allowed for the detection of *cis*-jasmone (**17**) in the culture (Fig. 7e). Due to the low endogenous *cis*-jasmone (**17**) levels in the yeast chassis, we supplied exogenous *cis*-jasmone (**17**) and proceeded to build the jasmolone (**18**) synthesis module in strain J2. Jasmolone (**18**) formation relies on the cytochrome P450 enzyme TcJMH, whose activity can be influenced by the choice of cytochrome P450 reductase (CPR). We therefore screened various plant-derived CPRs, including TcCPR, AaCPR[49], and SaCPR[49,50], using whole-cell biocatalysis assays. The combination of *TcJMH* with *SaCPR* showed the highest catalytic efficiency (Fig. 7f). Consequently, two copies of *SaCPR* and *TcJMH* were integrated into the genome of J2, yielding strain J3 (Supplementary Table S13), which efficiently converted fed *cis*-jasmone (**17**) into jasmolone (**18**) (Fig. 7g).

In Module III, we integrated a single copy of *TcUGT6* and *TcGLIP* into J3 to generate strain J4 (Fig. 7h; Supplementary Table S13). While this strain produced chrysanthemoyl-glucoside (**8**), the majority of chrysanthemic acid (**4**) remained unglycosylated (Supplementary Fig. S34). This low glycosylation efficiency of chrysanthemic acid (**4**) likely accounts for the absence of the final product jasmolin I (**21**) at this stage. To improve glycosylation efficiency for the subsequent condensation step, we introduced an additional copy of *TcUGT6* together with the yeast phosphoglucomutase gene *PGM1*, which promotes UDP-glucose accumulation into the *SPR1* locus[51]. Deletion of the endogenous glucosidase *SPR1*[52] was also performed to potentially reduce product degradation. The resulting strain J5 exhibited markedly improved glycosylation efficiency, with chrysanthemoyl-glucoside (**8**) accumulation increasing by approximately 4.6-fold relative to J4. Reduced product toxicity further elevated the titer of this glycosylated compound (Fig. 7h; Supplementary Fig. S34). Moreover, jasmolin I (**21**) was successfully detected in J5, with a titer of 0.55 mg/L (Supplementary Figs. S35, S36 and Table S13). Furthermore, to lower fermentation costs, we knocked out *GAL80*, a negative regulator of galactose metabolism[53] and added an extra copy of *TcGLIP*, creating the final production strain J6 (Supplementary Table S13). Fed with *cis*-jasmone (**17**), J6 successfully produced jasmolin I (**21**) at a titer of 1.22 mg/L in shake-flask fermentation, representing an approximately 2.2-fold improvement over J5 (Fig. 7i; Supplementary Fig. S35).

DISCUSSION

Over the past two decades, the biosynthetic pathways of several iconic plant terpenoids, paclitaxel[54,55], artemisinin[56], and cannabinol[57], have been elucidated, enabling synthetic-biology routes to plant-derived medicines. Here we extend this paradigm to botanical insecticides. We resolved three previously unidentified elements of the pyrethrin pathway and, on this basis, achieved heterologous production of jasmolin I (**21**) both in *N. benthamiana* and in *S. cerevisiae* upon supplementation with specific precursors. A bio-based route to natural pyrethrins thus points toward a potentially more sustainable alternative to chemically synthesized pyrethroids, whose widespread use has accelerated pest resistance and harmed non-target organisms.

Our pathway elucidation began from a catalytic bottleneck. Previous studies enhanced DMAPP (**1**) supply for chrysanthemic acid (**4**) biosynthesis in *E. coli* (15.30 mg/L in flasks, 141.78 mg/L in bioreactors)[22] and developed an isopentenol utilization pathway yielding 510 mg/L chrysanthemol[23]. Yet in the high-DMAPP yeast chassis JCR27[26,27], TcCDS alone produced no detectable chrysanthemol (**3**) (Fig. 3b), implicating inefficient dephosphorylation of the CDP (**2**) intermediate. We therefore hypothesized that plant TPS may harbor unrecognized dephosphorylating activity and identified TcTPS1 (Fig. 3c). Co-expression of *TcCDS* and *TcTPS1* substantially improved conversion of DMAPP (**1**) to chrysanthemol (**3**) in yeast (Fig. 3c), *E. coli* (Fig. 3d, e) and *N. benthamiana* (Fig. 3f). Although TcTPS1 may not be the optimal native enzyme in pyrethrum, it raises catalytic throughput and limits toxic intermediate accumulation. The "TcCDS + TcTPS1" module thus overcomes the core catalytic bottleneck in chrysanthemic acid (**4**) biosynthesis and provides a broadly applicable strategy for heterologous production of chrysanthemol (**3**), chrysanthemic acid (**4**) and, ultimately, pyrethrins.

Although β-oxidation is highly conserved in eukaryotes including yeast[58], TcACX3 from pyrethrum exhibits distinctive catalytic properties. Whereas *cis*-jasmone (**17**) is reported to arise via conventional β-oxidation of *iso*-OPDA (**14**) in various plants and yeast[38], the expected products from *cis*-OPDA (**13**) and *iso*-OPDA (**14**) should be 4,5-ddh-JA (**15**) and 3,7-ddh-JA (**16**), respectively. Our screening showed that TcACX3 selectively acts on *cis*-OPDA (**13**) while simultaneously mediating double-bond isomerization, without acting directly on *iso*-OPDA (**14**) (Fig. 4d); isotope-labeling experiments confirmed this substrate preference (Fig. 4e). Systematic evolutionary analysis showed that most *ACX* genes in pyrethrum (e.g., *TcACX5*, *TcACX7*, *TcACX8*, and *TcACX9*) arose by tandem duplication (Supplementary Fig. S11), whereas *TcACX3* did not. Instead, it is specifically retained in the pyrethrum lineage but lost from other closely related Asteraceae species (Supplementary Fig. S37). This lineage-specific evolution history likely underlies the specialized activity of TcACX3 toward *cis*-OPDA (**13**), and structural characterization will be needed for mechanistic insight.

In this study, we found that the acid moiety is activated by glycosylation: TcUGT1 and TcUGT6 convert chrysanthemic acid (**4**) into chrysanthemoyl-glucoside (**8**) (Fig. 5e, f), whereas chrysanthemoyl-CoA (**7**) was not detectable *in planta* (Supplementary Fig. S24e, f). Since TcGLIP is also active with chrysanthemoyl-CoA (**7**), however, we cannot formally exclude a CoA-dependent activation of the acid moiety, and a low-abundance or rapidly turned-over chrysanthemoyl-CoA (**7**) pool in glandular trichomes remains possible. Glycosylation therefore appears to serve as a prerequisite activation step for condensation, analogous to the situations reported in nicotine and littorine biosynthesis[47,59,60]. Notably, GLIP displays an unusual substrate promiscuity, accepting both chrysanthemoyl-glucoside (**8**) and chrysanthemoyl-CoA (**7**) for ester formation. Definitive assignment of the *in planta* acyl donor will require loss- or gain-of-function analysis in

T. cinerariifolium, which remains an important direction for future studies.

Synteny analysis revealed the absence of conserved *TcCDS* homologs in several closely related Asteraceae species, and phylogenetic evidence indicated that *TcCDS* originated from a recent whole-genome duplication (WGD) event in *T. cinerariifolium*, evolving from a farnesyl diphosphate synthase gene (Supplementary Figs. S37, S38 and Table S17). Microsynteny analysis of six core genes in the pyrethrin pathway (*TcTPS1*, *TcCDS*, *TcACX3*, *TcJMH*, *TcUGT6*, and *TcGLIP*) further showed that only *TcTPS1*, *TcUGT6*, and *TcGLIP* likely evolved through gene duplication events shared among Asteraceae species (Supplementary Fig. S37). By contrast, *TcCDS*, *TcACX3*, and *TcJMH* appear specifically retained in pyrethrum and lost in the other four closely related Asteraceae lineages, suggesting lineage-specific recruitment (Supplementary Fig. S37). Collectively, these findings illustrate how specialized metabolic pathways in non-model plants often arise through lineage-specific gene recruitment and functional innovation, revealing a reservoir of enzymatic diversity beyond the canonical pathways characterized in model species.

In summary, by demonstrating that TcTPS1 enhances the catalytic efficiency of TcCDS, elucidating the pyrethrum-specific β-oxidation route from *cis*-OPDA (**13**) to *cis*-jasmone (**17**), and revealing glycosylation of the acid moiety prior to condensation, we achieved the biosynthesis of pyrethrins in both *N. benthamiana* and *S. cerevisiae* (Supplementary Fig. S39). Beyond providing a new paradigm for heterologous synthesis, our findings highlight how evolutionary innovation in specialized enzymes drives natural-product diversity and underscore that plant metabolism still harbors a vast repertoire of uncharacterized enzymes with specialized functions.

MATERIAL AND METHODS

Plant materials

T. cinerariifolium plant samples were collected from Yuxi City (24° 20′ 49″ N, 102° 31′ 37″ E), Yunnan Province, China. Fresh leaves, stems, roots, and flower tissues were harvested and immediately frozen in liquid nitrogen, then stored at −80 °C prior to genome sequencing, transcriptome sequencing, and metabolite analysis. *N. benthamiana* plants were cultivated in an artificial climate chamber at 23 °C with a 16-h light/8-h dark cycle. Before Agrobacterium infection, *N. benthamiana* plants grew for about 4 weeks with regular watering.

Chemicals

All solvents used for extractions, chemical synthesis and preparative HPLC were of HPLC grade and purchased from Fisher Scientific. Chrysanthemol (**3**, CAS: 5617-92-5), chrysanthemic acid (**4**, CAS: 4638-92-0), α-LeA (**10**, CAS: 463-40-1), *cis*-OPDA (**13**, CAS: 85551-10-6) and *cis*-jasmone (**17**, CAS: 488-10-8) standards were purchased from Sigma-Aldrich. Compounds that were not commercially available were synthesized according to the procedures described in the Chemical Synthesis section of the Supplementary Materials.

Genome sequencing, assembly, and annotation

High-quality genomic DNA was isolated from fresh leaves by a modified CTAB method. PacBio HiFi (SMRTbell Express Template Prep Kit 2.0, Revio), 150-bp paired-end Illumina (NovaSeq 6000), and Hi-C libraries were prepared and sequenced following standard protocols. Total RNA from three replicates of roots, stems, leaves and flowers (stages S2, S4, S6) was extracted with TRIzol (Invitrogen) and used for PacBio Iso-Seq (Sequel, P6C4) and Illumina RNA-seq (NEBNext Ultra II RNA Kit, HiSeq 6000).

Hifiasm (v0.16.1) was used for self-correction and assembly with default parameters[61]. Assemblies were polished for two rounds with Pilon (v1.23)[62], and purge_dups (v1.2.5) removed duplications and reassigned allelic contigs. Scaffolds were anchored into chromosome-level scaffolds from Hi-C data with Juicer (v1.6)[63] and 3D-DNA (v180922)[64]. Assembly quality was assessed with BUSCO (v5.4.7)[65] and QUAST[66], and overall alignment rates were calculated after mapping HiFi, Iso-Seq, Illumina, assembled-transcript and RNA-seq reads with BWA (v0.7.13)[67], minimap2 (v2.17)[68], and HISAT2 (v2.1.0)[69]. Detailed procedures are provided in the Supplementary Materials and Methods.

Genome annotation

Gene prediction combined PacBio Iso-Seq data (Iso-Seq pipeline)[70] with open reading frames identified by TransDecoder (v5.5.0). For repeat annotation, both homology-based and *de novo* approaches were used: *de novo* identification with RepeatModeler (v2.0.3)[71], LTR retrotransposon prediction with LTR_Finder (v1.07)[72] and LTRharvest[73] and redundancy removal with LTR_retriever (v2.9.0)[74]; these sequences were combined with RepBase[75] as a library for RepeatMasker (v4.1.2)[76], and tandem repeats were identified with Tandem Repeat Finder (v4.09)[77].

Gene structures were annotated by integrating homology-based (miniprot), *ab initio* (GeneMark-ET v4.71[78], Augustus v3.3.3[79]) and RNA-seq-based (HISAT2[69], StringTie v2.0.6[80], TransDecoder (v5.5.0) predictions with Evidence Modeler (v2.0.0)[81]. Functional annotation was performed against Pfam, NR, SwissProt, TrEMBL[82] and KEGG with an *E*-value threshold of 1×10^{-5}; motifs, domains and Gene Ontology terms were assigned with InterProScan (v5.66-98.0)[83].

Gene family and evolutionary analysis

Genome-wide gene families were identified with OrthoFinder[84] for pyrethrum and eleven other plant species: *A. annua*[85], *A. thaliana*[86], *Amborella trichopoda*[87], *C. lavandulifolium*[88], *Chrysanthemum nankingense*[89], *Helianthus annuus*[90], *Mentha suaveolens*[91], *N. benthamiana*[92], *Taraxacum mongolicum*[93], *Jasminum sambac*[94] and *Vitis vinifera*[95]. Genome and protein sequences were retrieved from public databases. A maximum-likelihood species tree was constructed with RAxML (PROTGAMMAWAG)[96] from single-copy orthologs shared by all twelve species. Gene-family expansion and contraction were analyzed with CAFE[97] under default settings using a birth–death model. KEGG enrichment was performed for pyrethrum-specific and expanded gene families, and divergence times were estimated with the mcmctree program in PAML[98].

WGD analysis

The synonymous substitution rate (*Ks*) method was used to

identify WGD events by plotting intra- and inter-species *Ks* distributions. Protein sequences were aligned using BLAST and syntenic blocks detected with MCScanX[99]. Paralogous and orthologous gene pairs within these blocks were used to calculate *Ks*, the nonsynonymous substitution rate (*Ka*), and the *Ka*/*Ks* ratio with the yn00 module in PAML[98], and density plots of *Ks* values were generated.

Transcriptomic and co-expression analysis

Transcript expression was quantified with HISAT2[69] and FPKM (fragments per kilobase of transcript per million mapped reads) values were calculated from gene length and mapped read counts. A gene co-expression network was constructed with the R package WGCNA[100] from the expression of identified pathway genes. Functionally characterized genes (*TcCDS*, *TcGLIP*, and *TcJMH*) and the tissue-specific acid-moiety and pyrethrin contents were used as targets for Pearson correlation screening (correlation coefficient ≥ 0.7, $p \leq 0.05$).

Metabolite analysis of *T. cinerariifolium*

To quantify pyrethrin-pathway intermediates, leaves, stems, roots and flowers were ground into powder in liquid nitrogen; 100 mg of powder was extracted with 1 mL ethyl acetate by sonication for 15 min. The homogenate was centrifuged at 13,000 × *g* for 10 min, and the supernatant was concentrated under a nitrogen stream to 200 µL. After a further centrifugation, the supernatant was used for GC-MS and LC-MS analysis.

For GC-MS, an Agilent 8890 GC coupled to a 7000E TQ-MS was used with a DB-5Q column (30 m × 0.25 mm × 0.25 µm). The temperature program was: 50 °C (1 min), 15 °C/min to 110 °C, 6 °C/min to 200 °C (hold 1 min), 10 °C/min to 280 °C (total 30.33 min). Injection volume: 1 µL; split ratio: 15:1; injection port: 240 °C; MS scan: 45–500 *m*/*z*. High-resolution GC-Orbitrap (Thermo Scientific GC 240 coupled to Orbitrap Exploris) was used for precise mass confirmation (resolution 60,000; mass tolerance 5 ppm).

For LC-MS, supernatants were filtered through a 0.22 µm PTFE syringe filter before injection on an Agilent 1290 Infinity LC coupled to a 6475 triple-quadrupole mass spectrometer with a C18 column (250 mm × 4.6 mm, 5 µm) and a 3 µL injection. The mobile phase: 0.1% formic acid in water (A) and acetonitrile with 0.1% formic acid (B); gradient: 10%→60% B (0–15 min), 60%→95% B (15–25 min), 95% B (25–32 min), 95%–10% B (32–32.1 min), 10% B (32.1–40 min). Flow rate: 0.4 mL/min; column temperature: 40 °C. TQ-MS operated in full-scan mode (50–500 *m*/*z*, 300 ms) in positive and negative ion modes. To detect chrysanthemyl-CoA compounds, tissues were ground in liquid nitrogen and extracted with 80% methanol/water, sonicated on ice for 30 min, and centrifuged at 10,000 × *g* for 10 min. The filtered extract was analyzed by high-resolution LC-MS/MS on a Thermo UPLC system coupled to a Q Exactive Plus with an ACQUITY UPLC BEH C18 column (100 mm × 2.1 mm, 1.7 µm) at 45 °C, using the same mobile phases with a linear gradient, flow rate 0.4 mL/min and 1 µL injection, in negative HESI mode (100–1500 *m*/*z*).

Identification and cloning of candidate genes

Candidate genes involved in pyrethrin biosynthesis were identified by Hidden Markov Model[29] searches using corresponding Pfam IDs (LOX: PF00305; AOC: PF06351; ACX: PF01756; KAT: PF02803/PF00108; ACS: PF00501; SCPL: PF00450; CYP450: PF00067; UGT: PF00201), and by BLAST against reported homologs; protein sequences were aligned with MAFFT (v7.475)[101]. Phylogenetic trees were constructed using IQ-TREE[102] (see Supplementary Table S16 for the UGT tree). Full-length candidate genes were amplified from cDNA with Phanta Max Super-Fidelity (Vazyme) or PrimeSTAR GXL (Takara) using primers in Supplementary Table S15. For transient expression, PCR products were cloned into a modified pEAQ vector (*Xho*I/*Sal*I) and transformed into *Agrobacterium tumefaciens* GV3101; for heterologous expression in *E. coli*, CDSs were cloned into pET28a and transformed into DH5α and then Rosetta cells. Genes codon-optimized for *S. cerevisiae* were synthesized by GenScript Co., Ltd. (China).

Agrobacterium-mediated transient expression in *N. benthamiana*

Plasmids were transformed into *A. tumefaciens* GV3101 and grown on selective LB. Positive transformants were cultured, pelleted at 4,000 × *g*, resuspended in induction buffer (10 mmol/L MES, 10 mmol/L $MgCl_2$, 100 µmol/L acetosyringone, pH 5.6) and incubated for 1–2 h; suspensions were adjusted to OD_{600} = 0.4–0.6 (mixed at equal concentrations for combinations) and infiltrated into the abaxial side of 4–5-week-old leaves (three leaves from three plants per mixture). For substrate co-infiltration, plants were maintained until 3 days post-infiltration; substrate (100 ppm in water with 1% DMSO) was infiltrated into the infected region. Leaves were harvested 1 day later, snap-frozen, and stored at −80 °C. This system was used throughout for *in vivo* pathway validation.

Heterologous expression and enzymatic assays in *E. coli*

Chemically competent Rosetta cells were transformed with pET28a constructs and selected on chloramphenicol and kanamycin. Cultures were subcultured until OD_{600} ≈ 0.6, and induced with 0.1 mmol/L IPTG at 18 °C overnight. Cells were harvested at 3,000 × *g*, resuspended in 50 mmol/L sodium phosphate (pH 8.0), and disrupted by sonication, then used directly or stored at −80 °C. For crude-enzyme reactions, 1 mmol/L $MgCl_2$, 1 mmol/L substrate, and cofactors were added to 1 mL crude extract, incubated at 30 °C for 24 h, and quenched with 1 mL ethyl acetate. For purified TcCDS, TcTPS1, TcUGT6, and TcGLIP, lysates were purified on Ni^{2+}-NTA resin (250 mmol/L imidazole elution) and checked by SDS-PAGE; standard 100 µL reactions contained 100 µg enzyme, 150 µmol/L substrate, 1 mmol/L $MgCl_2$, 2 mmol/L DTT, 12.5% glycerol, 0.1% Tween-20 and 1 mmol/L ascorbic acid in 50 mmol/L Tris-HCl (pH 7.5) at 30 °C for 12 h with an empty-vector control, then quenched and analyzed by untargeted GC-MS, and kinetics were fitted with GraphPad Prism.

Chrysanthemoyl-glucoside (**8**) was synthesized enzymatically with purified recombinant TcUGT6. Chrysanthemic acid (2 mmol/L) was incubated with UDP-glucose (4 mmol/L) and purified TcUGT6 in 50 mmol/L Tris-HCl (pH 7.5) containing 1 mmol/L $MgCl_2$ and 2 mmol/L DTT (total 1 mL) at 30 °C for 12 h. The reaction was quenched with methanol, desalted by C18 solid-phase extraction, and purified by semi-preparative reversed-phase HPLC (Eclipse XDB-C18, 9.4 mm × 250 mm, 5 µm). The target fraction was lyophilized and redissolved

in methanol; the identity of **8** was confirmed by LC-MS/MS ([M+HCOOH−H]$^-$, *m/z* = 375.1), and it was stored at −80 °C as the acyl donor for TcGLIP assays.

Protein crystal modeling

The three-dimensional structure of the target protein was predicted using AlphaFold3[103], and molecular docking was performed with AutoDock Vina 1.2.3[104]. Generated poses were ranked by binding free energy (ΔG), and the top-ranked pose was selected. The binding mode of the protein-ligand complex was visualized in PyMOL 3.0.0 (pymol.org/pymol.html); the receptor was shown as a cartoon, key pocket residues and the ligand as sticks, and non-covalent interactions such as hydrogen bonds were annotated with PyMOL tools.

Modular engineering for heterologous biosynthesis in *S. cerevisiae*

The *S. cerevisiae* strain JCR27[26], engineered to boost terpenoid production, was the parent for chrysanthemic acid, and strain 30000B for 3,7-ddh-JA (Supplementary Tables S13, S14). DNA was transformed by the LiAc/SS carrier DNA/PEG method[105], with mutants confirmed by colony PCR. For growth and heterologous production, colonies were grown in 4 mL synthetic drop-out medium (30 °C, 220 rpm) and transferred to 50 mL YPDG at OD_{600} = 0.1 and incubated 3–5 days before extraction. For whole-cell biotransformation, cells grown to OD_{600} ≈ 5.0 were pelleted at 3,000 × *g*, resuspended in 1 mL 50 mmol/L potassium phosphate (pH 7.4), and incubated with substrate at 30 °C, 220 rpm; products were extracted with 1 mL ethyl acetate and analyzed by GC-MS. Pathway genes were integrated module-by-module to achieve *de novo* chrysanthemic acid synthesis, followed by precursor feeding with *cis*-jasmone to produce jasmolin I, following established procedures[27].

DATA AVAILABILITY

All raw sequence and genome assembly data in this study have been deposited in the National Genomics Data Center (ngdc.cncb.ac.cn) with BioProject accession numbers PRJCA053112 and PRJCA027806.

ACKNOWLEDGEMENTS

This work was supported by Shanghai Municipal Science and Technology Major Project to T.L., grants from the National Natural Science Foundation of China to T.L. (U23A20527, W251201100) and Y.L. (32600348), the Project of State Key Laboratory of Microbial Metabolism, Shanghai Jiao Tong University to T.L. (SKLMMZD_08), and sponsored by the AI for Science Seed Program of Shanghai Jiao Tong University (2025AI4S-QY08). The numerical calculations in this paper have been done on the supercomputing system in the Supercomputing Center of Wuhan University. The Core Facility and Service Center (CFSC) of the School of Life Sciences and Biotechnology, Shanghai Jiao Tong University, provided technical support for the high-resolution mass spectrometry analysis.

AUTHOR CONTRIBUTIONS

Y.L., X.X., S.W., Y.Z., F.C., Y.Y., X.F., J.Y., R.L., and D.Y. performed the experiments; K.L., Q.J., K.S., A.H., and Z.D. provided experimental materials; T.L. and L.L. conceived the project, designed the experiments, and prepared the manuscript. All authors read and approved the final manuscript.

COMPETING INTERESTS

Z.D. serves as Editor-in-Chief of this journal and T.L. serves as Executive Editor-in-Chief of this journal. They were not involved in the editorial review or decision-making process for this manuscript. All editorial decisions were made independently by other members of the Editorial Board who have no conflicts of interest. T.L. is applying for patents based on this research. All remaining authors and Yunnan Nanbao Biotechnology Co., Ltd. declare no competing interests.

REFERENCES

1. Staudinger, H. & Ruzicka, L. Insektentötende stoffe I. Über isolierung und konstitution des wirksamen teiles des dalmatinischen insektenpulvers. *Helv. Chim. Acta.* **7**, 177–201 (1924).
2. Antonious, G. F. Residues and half-lives of pyrethrins on field-grown pepper and tomato. *J. Environ. Sci. Health. Part. B.* **39** , 491–503 (2004).
3. Pan, L., Feng, X. & Zhang, H. Dissipation and residues of pyrethrins in leaf lettuce under greenhouse and open field conditions. *Int. J. Environ. Res. Public. Health.* **14** , 822 (2017).
4. Kumar, A., Jasrotia, S., Dutta, J. & Kyzas, G. Z. Pyrethroids toxicity in vertebrates and invertebrates and amelioration by bioactive compounds: a review. *Pestic. Biochem. Physiol.* **196**, 105615 (2023).
5. Sen, K. et al. Pyrethroids in sustainable environment: a natural product for crop protection. *Environ. Qual. Manag.* **36**, e70466 (2026).
6. Duchon, S., Bonnet, J., Marcombe, S., Zaim, M. & Corbel, V. Pyrethrum: a mixture of natural pyrethrins has potential for malaria vector control. *J. Med. Entomol.* **46** , 516–522 (2009).
7. Anderson, J. F. & Cowles, R. S. Susceptibility of *Cimex lectularius* (Hemiptera: Cimicidae) to pyrethroid insecticides and to insecticidal dusts with or without pyrethroid insecticides. *J. Econ. Entomol.* **105**, 1789–1795 (2012).
8. Scott, J. G. et al. Insecticide resistance in house flies from the United States: resistance levels and frequency of pyrethroid resistance alleles. *Pestic. Biochem. Physiol.* **107**, 377–384 (2013).
9. Kgoroebutswe, T. K., Ramatlho, P., Reeder, S., Makate, N. & Paganotti, G. M. Distribution of anopheles mosquito species, their vectorial role and profiling of knock-down resistance mutations in Botswana. *Parasitol. Res.* **119**, 1201–1208 (2020).
10. Evans, W. C., Evans, D. & Trease, G. E. Trease and evans pharmacognosy. 16th edn. Saunders/Elsevier, (2009).
11. Rivera, S. B. et al. Chrysanthemyl diphosphate synthase: isolation of the gene and characterization of the recombinant non-head-to-tail monoterpene synthase from *Chrysanthemum cinerariaefolium*. *Proc. Natl. Acad. Sci. U. S. A.* **98**, 4373–4378 (2001).
12. Li, W. et al. A trichome-specific, plastid-localized *Tanacetum cinerariifolium* nudix protein hydrolyzes the natural pyrethrin pesticide biosynthetic intermediate *trans*-chrysanthemyl diphosphate. *Front. Plant. Sci.* **11**, 482 (2020).
13. Xu, H. et al. Coexpression analysis identifies two oxidoreductases involved in the biosynthesis of the monoterpene acid moiety of natural pyrethrin insecticides in *Tanacetum cinerariifolium*. *Plant. Physiol.* **176**, 524–537 (2018).
14. Xu, H. et al. Pyrethric acid of natural pyrethrin insecticide: complete pathway elucidation and reconstitution in *Nicotiana benthamiana*. *New. Phytol.* **223**, 751–765 (2019).
15. Inoue, S., Tsuzuki, H., Matsuda, K., Kitaoka, N. & Matsuura, H. Investigation of the biosynthesis pathway that generates *cis*-jasmone. *ChemBioChem.* **25**,

e202300593 (2024).
16. Li, W., Zhou, F. & Pichersky, E. Jasmone hydroxylase, a key enzyme in the synthesis of the alcohol moiety of pyrethrin insecticides. *Plant. Physiol.* **177**, 1498–1509 (2018).
17. Li, W., Lybrand, D. B., Zhou, F., Last, R. L. & Pichersky, E. Pyrethrin biosynthesis: the cytochrome P450 oxidoreductase CYP82Q3 converts jasmolone to pyrethrolone. *Plant. Physiol.* **181**, 934–944 (2019).
18. Kikuta, Y. et al. Identification and characterization of a GDSL lipase-like protein that catalyzes the ester-forming reaction for pyrethrin biosynthesis in *Tanacetum cinerariifolium*—a new target for plant protection. *Plant. J.* **71**, 183–193 (2012).
19. Sugisaka, Y., Aoyama, S., Kumagai, K., Ihara, M. & Matsuda, K. TcGLIP GDSL lipase substrate specificity co-determines the pyrethrin composition in *Tanacetum cinerariifolium*. *J. Agric. Food. Chem.* **70** , 8645–8652 (2022).
20. Xu, H. et al. Production of *trans*-chrysanthemic acid, the monoterpene acid moiety of natural pyrethrin insecticides, in tomato fruit. *Metab. Eng.* **47**, 271–278 (2018).
21. Wang, Y. et al. Engineering of tomato type VI glandular trichomes for *trans*-chrysanthemic acid biosynthesis, the acid moiety of natural pyrethrin insecticides. *Metab. Eng.* **72**, 188–199 (2022).
22. Yu, J. et al. Genome-scale metabolic modeling guided *Escherichia coli* engineering for *de novo* biosynthesis of chrysanthemic acid. *Adv. Sci. (Weinh).* **13**, e12736 (2026).
23. Liao, Z. et al. An enzyme cascade for green synthesis of chrysanthemol and chrysanthemic acid: key precursors for pyrethrins and pyrethroids. *Green. Chem.* **28** , 9983–9995 (2026).
24. Xu, Z. et al. TcbZIP60 positively regulates pyrethrins biosynthesis in *Tanacetum cinerariifolium*. *Front. Plant. Sci.* **14**, 1133912 (2023).
25. Zeng, T. et al. TcMYC2 regulates pyrethrin biosynthesis in *Tanacetum cinerariifolium*. *Hortic. Res.* **9**, uhac178 (2022).
26. Ma, T. et al. Lipid engineering combined with systematic metabolic engineering of *Saccharomyces cerevisiae* for high-yield production of lycopene. *Metab. Eng.* **52**, 134–142 (2019).
27. Zhi, Y. et al. Gene-directed *in vitro* mining uncovers the insect-repellent constituent from mugwort (*Artemisia argyi*). *J. Am. Chem. Soc.* **146**, 30883–30892 (2024).
28. Li, Q. et al. Phylogeny and functional differentiation of the terpene synthase gene family in angiosperms with emphasis on *Rosa chinensis*. *Int. J. Mol. Sci.* **26** , 2113 (2025).
29. Eddy, S. What is a hidden markov model? *Nat. Biotechnol.* **22**, 1315–1316 (2004).
30. Chen, F., Tholl, D., Bohlmann, J. & Pichersky, E. The family of terpene synthases in plants: a mid-size family of genes for specialized metabolism that is highly diversified throughout the kingdom. *Plant. J.* **66**, 212–229 (2011).
31. Yang, T. et al. Chrysanthemyl diphosphate synthase operates *in planta* as a bifunctional enzyme with chrysanthemol synthase activity. *J. Biol. Chem.* **289**, 36325–36335 (2014).
32. Xu, Z. et al. Systematic identification of terpene synthases from sacred lotus (*Nelumbo nucifera*) and heterologous biosynthesis of the insecticidal and antimicrobial compound γ-eudesmol. *Hortic. Res.* **12**, uhaf191 (2025).
33. Demissie, Z. A., Erland, L. A., Rheault, M. R. & Mahmoud, S. S. The biosynthetic origin of irregular monoterpenes in *Lavandula*: isolation and biochemical characterization of a novel *cis*-prenyl diphosphate synthase gene, lavandulyl diphosphate synthase. *J. Biol. Chem.* **288**, 6333–6341 (2013).
34. Ignea, C., Pontini, M., Maffei, M. E., Makris, A. M. & Kampranis, S. C. Engineering monoterpene production in yeast using a synthetic dominant negative geranyl diphosphate synthase. *ACS. Synth. Biol.* **3**, 298–306 (2014).
35. Moraes, M. C. et al. *cis*-jasmone induces accumulation of defence compounds in wheat, *Triticum aestivum*. *Phytochemistry.* **69**, 9–17 (2008).
36. Birkett, M. A. et al. New roles for *cis*-jasmone as an insect semiochemical and in plant defense. *Proc. Natl. Acad. Sci. U. S. A.* **97** , 9329–9334 (2000).
37. Agbessenou, A., Akutse, K. S., Yusuf, A. A. & Khamis, F. M. The endophyte *Trichoderma asperellum* M2RT4 induces the systemic release of methyl salicylate and (*Z*)-jasmone in tomato plant affecting host location and herbivory of tuta absoluta. *Front. Plant. Sci.* **13**, 860309 (2022).
38. Dabrowska, P. & Boland, W. *iso*-OPDA: an early precursor of *cis*-jasmone in plants? *ChemBioChem.* **8**, 2281–2285 (2007).
39. Kajiwara, A., Abe, T., Hashimoto, T., Matsuura, H. & Takahashi, K. Efficient synthesis of (+)-*cis*-12-oxo-phytodienoic acid by an *in vitro* enzymatic reaction. *Biosci. Biotechnol. Biochem.* **76**, 2325–2328 (2012).
40. Tang, H., Lin, S., Deng, J., Keasling, J. D. & Luo, X. Engineering yeast for the *de novo* synthesis of jasmonates. *Nat. Synth.* **3**, 224–235 (2024).
41. Dabrowska, P., Shabab, M., Brandt, W., Vogel, H. & Boland, W. Isomerization of the phytohormone precursor 12-oxophytodienoic acid (OPDA) in the insect gut: a mechanistic and computational study. *J. Biol. Chem.* **286**, 22348–22354 (2011).
42. Dabrowska, P., Freitak, D., Vogel, H., Heckel, D. G. & Boland, W. The phytohormone precursor OPDA is isomerized in the insect gut by a single, specific glutathione transferase. *Proc. Natl. Acad. Sci. U. S. A.* **106**, 16304–16309 (2009).
43. Koo, A. J. & Howe, G. A. Role of peroxisomal β-oxidation in the production of plant signaling compounds. *Plant. Signal. Behav.* **2**, 20–22 (2007).
44. Wasternack, C. & Hause, B. Jasmonates: biosynthesis, perception, signal transduction and action in plant stress response, growth and development. An update to the 2007 review in Annals of Botany. *Ann. Bot.* **111**, 1021–1058 (2013).
45. Koch, T., Bandemer, K. & Boland, W. Biosynthesis of *cis*-jasmone: a pathway for the inactivation and the disposal of the plant stress hormone jasmonic acid to the gas phase? *Helv. Chim. Acta.* **80**, 838–850 (1997).
46. Zeng, J. et al. Discovering a mitochondrion-localized BAHD acyltransferase involved in calystegine biosynthesis and engineering the production of 3β-tigloyloxytropane. *Nat. Commun.* **15**, 3623 (2024).
47. Qiu, F. et al. Functional genomics analysis reveals two novel genes required for littorine biosynthesis. *New. Phytol.* **225**, 1906–1914 (2020).
48. Ma, A., Yu, H. & Li, A. Compartmentalized orthogonal biosynthesis for boosting limonene and oxygenated monoterpenoid production in *Saccharomyces cerevisiae*. *Bioresour. Technol.* **442**, 133686 (2026).
49. Wang, D. et al. Enhanced production of santalols by engineering the cytochrome P450 enzyme to the peroxisomal surface in yeast. *J. Agric. Food. Chem.* **73**, 20307–20316 (2025).
50. Zha, W. et al. Rationally engineering santalene synthase to readjust the component ratio of sandalwood oil. *Nat. Commun.* **13**, 2508 (2022).
51. Li, H., Ma, W., Lyv, Y., Gao, S. & Zhou, J. Glycosylation modification enhances (2S)-Naringenin production in *Saccharomyces cerevisiae*. *ACS. Synth. Biol.* **11**, 2339–2347 (2022).
52. Li, S. et al. Efficient conversion of stevioside to rebaudioside M in *Saccharomyces cerevisiae* by a engineering hydrolase system and prolonging the growth cycle. *J. Agric. Food. Chem.* **72**, 8140–8148 (2024).
53. Wu, Y. et al. Engineering an efficient expression using heterologous GAL promoters and transcriptional activators in *Saccharomyces cerevisiae*. *ACS. Synth. Biol.* **12**, 1859–1867 (2023).
54. McClune, C. J. et al. Discovery of *FoTO1* and *Taxol* genes enables biosynthesis of baccatin III. *Nature.* **643**, 582–592 (2025).
55. Liang, F. et al. Elucidation of the final steps in Taxol biosynthesis and its biotechnological production. *Nat. Synth.* **4**, 1212–1222 (2025).
56. Guo, Z. et al. Dihydroartemisinic acid dehydrogenase-mediated alternative route for artemisinin biosynthesis. *Nat. Commun.* **16**, 3888 (2025).
57. Berman, P. et al. Parallel evolution of cannabinoid biosynthesis. *Nat. Plants.* **9**, 817–831 (2023).
58. Wang, Z. et al. Key enzymes involved in the utilization of fatty acids by *Saccharomyces cerevisiae*: a review. *Front. Microbiol.* **14**, 1294182 (2023).
59. Schwabe, B. T. W. et al. Nicotine biosynthesis is completed by cryptic activating glucosylation. *Nat. Commun.* **17**, 4221 (2026).
60. Chang, L. et al. Complete biosynthesis of nicotine. *Cell.* **189**, 2700–2713 (2026).

61. Cheng, H., Concepcion, G., Feng, X., Zhang, H. & Li, H. Haplotype-resolved *de novo* assembly using phased assembly graphs with hifiasm. *Nat. Methods.* **18** , 170–175 (2021).
62. Walker, B. et al. Pilon: an integrated tool for comprehensive microbial variant detection and genome assembly improvement. *PLoS. One.* **9**, e112963 (2014).
63. Durand, N. C. et al. Juicer provides a one-click system for analyzing loop-resolution Hi-C experiments. *Cell. Syst.* **3**, 95–98 (2016).
64. Dudchenko, O. et al. *De novo* assembly of the Aedes aegypti genome using Hi-C yields chromosome-length scaffolds. *Science.* **356**, 92–95 (2017).
65. Manni, M., Berkeley, M. R., Seppey, M., Simão, F. A. & Zdobnov, E. M. BUSCO update: novel and streamlined workflows along with broader and deeper phylogenetic coverage for scoring of eukaryotic, prokaryotic, and viral genomes. *Mol. Biol. Evol.* **38**, 4647–4654 (2021).
66. Mikheenko, A., Prjibelski, A., Saveliev, V., Antipov, D., & Gurevich, A. Versatile genome assembly evaluation with QUAST-LG. *Bioinformatics.* **34** , i142–i150 (2018).
67. Li, H. & Durbin, R. Fast and accurate short read alignment with Burrows–Wheeler transform. *Bioinformatics.* **25**, 1754–1760 (2009).
68. Li, H. Minimap2: pairwise alignment for nucleotide sequences. *Bioinformatics.* **34**, 3094–3100 (2018).
69. Kim, D., Paggi, J. M., Park, C., Bennett, C., & Salzberg, S. L. Graph-based genome alignment and genotyping with HISAT2 and HISAT-genotype. *Nat. Biotechnol.* **37**, 907–915 (2019).
70. Guizard, S. et al. nf-core/isoseq: simple gene and isoform annotation with PacBio Iso-Seq long-read sequencing. *Bioinformatics.* **39**, btad150 (2023).
71. Flynn, J.M. et al. RepeatModeler2 for automated genomic discovery of transposable element families. *Proc. Natl. Acad. Sci. U. S. A.* **117**, 9451–9457 (2020).
72. Xu, Z. & Wang, H. LTR_FINDER: an efficient tool for the prediction of full-length LTR retrotransposons. *Nucleic. Acids. Res.* **35**, W265–268 (2007).
73. Ellinghaus, D., Kurtz, S. & Willhoeft, U. LTRharvest, an efficient and flexible software for *de novo* detection of LTR retrotransposons. *BMC. Bioinformatics.* **9**, 18 (2008).
74. Ou, S. & Jiang, N. LTR_retriever: a highly accurate and sensitive program for identification of long terminal repeat retrotransposons. *Plant. Physiol.* **176**, 1410–1422 (2018).
75. Bao, W., Kojima, K. K. & Kohany, O. Repbase update, a database of repetitive elements in eukaryotic genomes. *Mob. DNA.* **6**, 11 (2015).
76. Tarailo-Graovac, M. & Chen, N. Using RepeatMasker to identify repetitive elements in genomic sequences. *Curr. Protoc. Bioinformatics.* **4**, 4.10.11–14.10.14 (2009).
77. Benson, G. Tandem repeats finder: a program to analyze DNA sequences. *Nucleic. Acids. Res.* **27**, 573–580 (1999).
78. Lomsadze, A., Burns, P. D. & Borodovsky, M. Integration of mapped RNA-seq reads into automatic training of eukaryotic gene finding algorithm. *Nucleic. Acids. Res.* **42**, e119 (2014).
79. Stanke, M. et al. AUGUSTUS: ab initio prediction of alternative transcripts. *Nucleic. Acids. Res.* **34**, W435–439 (2006).
80. Pertea, M. et al. StringTie enables improved reconstruction of a transcriptome from RNA-seq reads. *Nat. Biotechnol.* **33**, 290–295 (2015).
81. Haas, B.J. et al. Automated eukaryotic gene structure annotation using EVidenceModeler and the program to assemble spliced alignments. *Genome. Biol.* **9**, R7 (2008).
82. Boeckmann, B. et al. The SWISS-PROT protein knowledgebase and its supplement TrEMBL in 2003. *Nucleic. Acids. Res.* **31**, 365–370 (2003).
83. Jones, P. et al. InterProScan 5: genome-scale protein function classification. *Bioinformatics.* **30**, 1236–1240 (2014).
84. Emms, D.M. & Kelly, S. OrthoFinder: phylogenetic orthology inference for comparative genomics. *Genome. Biol.* **20**, 238 (2019).
85. Shen, Q. et al. The genome of *Artemisia annua* provides insight into the evolution of asteraceae family and artemisinin biosynthesis. *Mol. Plant.* **11**(6), 776–788 (2018).
86. The Arabidopsis Genome Initiative. Analysis of the genome sequence of the flowering plant *Arabidopsis thaliana*. *Nature.* **408**, 796–815 (2000).
87. DePamphilis, C. W. et al. The Amborella genome and the evolution of flowering plants. *Science.* **342**, 1241089 (2013).
88. Wen, X. et al. The *Chrysanthemum lavandulifolium* genome and the molecular mechanism underlying diverse capitulum types. *Hortic. Res.* **9**, uhab022 (2022).
89. Song, C. et al. The *Chrysanthemum nankingense* genome provides insights into the evolution and diversification of *Chrysanthemum* flowers and medicinal traits. *Mol. Plant.* **11**, 1482–1491 (2018).
90. Badouin, H. et al. The sunflower genome provides insights into oil metabolism, flowering and Asterid evolution. *Nature.* **546**, 148–152 (2017).
91. Firl, A. et al. Chromosome-scale assembly of apple mint (*Mentha suaveolens*). *BMC. Genom. Data.* **25**, 96 (2024).
92. Chen, W. et al. The complete genome assembly of *Nicotiana benthamiana* reveals the genetic and epigenetic landscape of centromeres. *Nat. Plants.* **10**, 1928–1943 (2024).
93. Lin, S. et al. Extensive sequence divergence between the reference genomes of *Taraxacum* kok-saghyz and *Taraxacum mongolicum*. *Sci. China. Life. Sci.* **65**, 515–528 (2022).
94. Wang, P. et al. Genomes of single- and double-petal jasmines (*Jasminum sambac*) provide insights into their divergence time and structural variations. *Plant. Biotechnol. J.* **20**, 1232–1234 (2022).
95. Shi, X. et al. The complete reference genome for grapevine (*Vitis vinifera* L.) genetics and breeding. *Hortic. Res.* **10**, uhad061 (2023).
96. Stamatakis, A. RAxML version 8: a tool for phylogenetic analysis and post-analysis of large phylogenies. *Bioinformatics.* **30**, 1312–1313 (2014).
97. De Bie, T., Cristianini, N., Demuth, J. P. & Hahn, M. W. CAFE: a computational tool for the study of gene family evolution. *Bioinformatics.* **22**, 1269–1271 (2006).
98. Yang, Z. PAML 4: phylogenetic analysis by maximum likelihood. *Mol. Biol. Evol.* **24**, 1586–1591 (2007).
99. Wang, J. et al. MCScanX: a toolkit for detection and evolutionary analysis of gene synteny and collinearity. *Nucleic. Acids. Res.* **40**, e49 (2012).
100. Langfelder, P. & Horvath, S. WGCNA: an R package for weighted correlation network analysis. *BMC. Bioinformatics.* **9**, 559 (2008).
101. Katoh, K., Misawa, K., Kuma, K. & Miyata, T. MAFFT: a novel method for rapid multiple sequence alignment based on fast Fourier transform. *Nucleic. Acids. Res.* **30**, 3059–3066 (2002).
102. Nguyen, L. T., Schmidt, H. A., von Haeseler, A. & Minh, B. Q. IQ-TREE: a fast and effective stochastic algorithm for estimating maximum-likelihood phylogenies. *Mol. Biol. Evol.* **32**, 268–274 (2015).
103. Abramson, J. et al. Accurate structure prediction of biomolecular interactions with AlphaFold 3. *Nature.* **630**, 493–500 (2024).
104. Trott, O. & Olson, A.J. AutoDock vina: improving the speed and accuracy of docking with a new scoring function, efficient optimization, and multithreading. *J. Comput. Chem.* **31**, 455–461 (2010).
105. Gietz, R.D. & Schiestl, R.H. High-efficiency yeast transformation using the LiAc/SS carrier DNA/PEG method. *Nat. Protoc.* **2**, 31–34 (2007).

ADDITIONAL INFORMATION

Supplementary information The online version contains supplementary material available at https://doi.org/10.2738/vita.microbiology.2026.10.0005.

Correspondence and requests for materials should be addressed to Li Lu and Tiangang Liu.

Reprints and permission information is available at https://www.vita-journal.com/microbiology.

© The Author(s) 2026. Published by Higher Education Press. This is an Open Access article distributed under the terms of the CC BY license (https://creativecommons.org/licenses/by/4.0/).